Subharmonic Energy Transfer from the Semidiurnal Internal Tide to Near-Diurnal Motions over Kaena Ridge, Hawaii

OLIVER M. SUN AND ROBERT PINKEL

Marine Physical Laboratory, Scripps Institution of Oceanography, La Jolla, California

(Manuscript received 31 July 2012, in final form 25 December 2012)

ABSTRACT

Nonlinear energy transfers from the semidiurnal internal tide to high-mode, near-diurnal motions are documented near Kaena Ridge, Hawaii, an energetic generation site for the baroclinic tide. Data were collected aboard the Research *Floating Instrument Platform* (*FLIP*) over a 35-day period during the fall of 2002, as part of the Hawaii Ocean Mixing Experiment (HOME) Nearfield program.

Energy transfer terms for a PSI resonant interaction at midlatitude are identified and compared to those for near-inertial PSI close to the M_2 critical latitude. Bispectral techniques are used to demonstrate significant energy transfers in the Nearfield, between the low-mode M_2 internal tide and subharmonic waves with frequencies near $M_2/2$ and vertical wavelengths of $O(120\ \text{m})$. A novel prefilter is used to test the PSI wavenumber resonance condition, which requires the subharmonic waves to propagate in opposite vertical directions. Depth–time maps of the interactions, formed by directly estimating the energy transfer terms, show that energy is transferred predominantly from the tide to subharmonic waves, but numerous reverse energy transfers are also found. A net forward energy transfer rate of 2×10^{-9} W kg^{-1} is found below 400 m.

The suggestion is that the HOME observations of energy transfer from the tide to subharmonic waves represent a first step in the open-ocean energy cascade. Observed PSI transfer rates could account for a small but significant fraction of the turbulent dissipation of the tide within 60 km of Kaena Ridge. Further extrapolation suggests that integrated PSI energy transfers equatorward of the M_2 critical latitude may be comparable to PSI energy transfers previously observed near 28.8°N.

1. Introduction

The overturning circulation of the World Ocean produces deep water at a rate of order 25 Sv (1 Sv $\equiv 10^6$ m s^{-1}). It has been estimated that about 2 TW of mechanical mixing works against this influx of cold, salty water to maintain the observed abyssal stratification, with most of the energy coming from the winds and tides (Munk and Wunsch 1998; Wunsch and Ferrari 2004). While these energy inputs act on spatial scales of tens to hundreds of kilometers, turbulent mixing occurs at subcentimeter scales. A downscale energy cascade is widely hypothesized, wherein energy is transferred from the large, energy-containing waves, through ever-smaller internal waves, and eventually to small-scale breaking waves associated with dissipation. Nonlinear wave–wave interactions are thought to play a key role in this internal wave energy cascade (Müller and Olbers 1975; McComas and Bretherton 1977; McComas and Müller 1981a; Müller et al. 1986; St. Laurent and Garrett 2002; Polzin 2004).

Resonant interactions between triads of oceanic waves were originally considered by Phillips (1960). Weakly nonlinear energy transfers are predicted between triads of internal waves whose wave vectors and frequencies $(\mathbf{k}_1, \omega_1)$, $(\mathbf{k}_2, \omega_2)$, $(\mathbf{k}_3, \omega_3)$ satisfy the resonance conditions

$$\mathbf{k}_1 + \mathbf{k}_2 = \mathbf{k}_3 \quad \text{and} \tag{1}$$

$$\omega_1 + \omega_2 = \omega_3 . \tag{2}$$

The theory was extended by Phillips (1961), Hasselmann (1962, 1963a,b), Bretherton (1964), Benney and Saffman (1966), and many others to analyze resonant interactions within continuous-spectrum wavefields, in which a multitude of triads may be simultaneously interacting.

McComas and Bretherton (1977) divided the triad interactions into three distinct classes, which they gave the names Induced Diffusion, Parametric Subharmonic

Corresponding author address: Oliver M. Sun, Woods Hole Oceanographic Institution, M.S. #21 Woods Hole, MA 02543.
E-mail: osun@whoi.edu

DOI: 10.1175/JPO-D-12-0141.1

Instability, and Elastic Scattering. Each class represents a limiting case in frequency or wavenumber scale separation between two of the triad members and the third. Induced Diffusion (ID) is an interaction between a pair of similar small-scale–high-frequency waves and a large-scale–low-frequency wave. Elastic Scattering (ES) transfers energy between two waves with nearly opposite vertical, but similar horizontal, wavenumbers. The third wave in ES has nearly double the vertical wavenumber (half the wavelength) of the other triad members and a small horizontal wavenumber.

The focus of this study is Parametric Subharmonic Instability (PSI), an interaction between a ''parent wave'' and a pair of ''daughter waves'' at close to half the frequency of the parent. The daughter waves, which have much smaller vertical scales than the parent, are able to fulfill the resonance condition (1) by having nearly opposite wave vectors. The large vertical scale separation but limited frequency separation between the triad members gives PSI a special relevance to the tidal energy cascade, as PSI can transfer energy directly from the low-mode, energy-containing tides to high-mode, shear-containing waves, which are much closer in scale to turbulent mixing processes. The net contribution of PSI to tidal decay and mixing remains poorly quantified, however.

Early theoretical studies of PSI in random-phase, near-Garrett–Munk (GM) (Munk 1981) oceanic wavefields predicted relatively long interaction time scales, of order 100 days, which suggested that PSI would not be detectible under typical ocean conditions (McComas and Müller 1981b; Olbers and Pomphrey 1981; Müller et al. 1986). Bicoherences reported by Neshyba and Sobey (1975) were attributed to kinematic effects rather than nonlinear energy transfers. More recently, there has been evidence that PSI of strong M_2 internal tides can take place over much shorter time scales. In particular, a series of numerical studies found PSI time scales of only a few days as the propagating M_2 internal tide approaches the critical latitude of 28.8°, where the half-frequency of the tide is exactly equal to the local inertial frequency f, and the subharmonic waves become locally trapped (Hibiya et al. 1998, 2002; MacKinnon and Winters 2005; Furuichi et al. 2005; Simmons 2008). An analytical theory for near-inertial PSI, developed by Young et al. (2008), predicted subharmonic growth rates similar to the numerical estimates of MacKinnon and Winters (2005).

Motivated by these results, the Internal Waves Across the Pacific (IWAP) experiment (Alford et al. 2007) attempted to observe the PSI decay of the M_2 internal tide as it propagates northward from the Hawaiian Ridge across the critical latitude. Elevated shear variances were reported equatorward of the critical latitude, and close to 28.8°N, near-inertial waves were observed in a characteristic standing pattern associated with PSI (Alford et al. 2007). The near-inertial waves were found to be significantly bicoherent with the M_2 tide (MacKinnon et al. 2012). However, PSI energy transfers inferred from dissipation estimates and the decay of the M_2 tide were only 10%–20% of the incoming tidal energy flux, rather than the 40% or more predicted by models (Alford et al. 2007; Simmons 2008; MacKinnon et al. 2012).

Although PSI is expected to act most efficiently near the critical latitude, it may also be energetically important elsewhere. Observations from the Hawaii Ocean Mixing Experiment (HOME) suggested that PSI is active near internal tidal generation sites. During an 11-day ship survey along Kaena Ridge, near 21.7°N, Carter and Gregg (2006) found pairs of near-diurnal waves resembling PSI subharmonics, which they found to be significantly bicoherent with a tidal beam emanating from the Ridge in a narrow 525–595-m-depth range. Frajka-Williams et al. (2006) also calculated bicoherences in HOME using a series of velocity profiles but deemed their results inconclusive because of limited sampling. At the HOME Farfield site, 430 km to the south–southwest of the ridge, Rainville and Pinkel (2006a) observed diurnal fluxes that varied more nearly with semidiurnal, rather than diurnal forcing, also suggesting the possible influence of PSI.

Meanwhile, in the North Atlantic Tracer Release Experiment (NATRE) survey area, at 24°–28°N and far from any significant internal tidal generation sites, Polzin and Lvov (2011) found unusually high spectral levels of high-wavenumber near-inertial energy, which they attributed to the PSI decay of a strong M_2 tidal peak. Similarly, in numerical simulations, Furuichi et al. (2005) found elevated PSI energy transfers in a ~5° band between 25° and 30°N.

In this study, we attempt to further document PSI energy transfers from the semidiurnal internal tide to near-diurnal subharmonics near Kaena Ridge, Hawaii. We consider data collected during a six-week deployment of the *Floating Instrument Platform* (*FLIP*), as part of the 2002 HOME Nearfield component, spanning a 35-day period and containing more than 11 000 profiles of density and horizontal velocity covering depths of 15–800 m. Because of the spatial and temporal variability of the internal wave field near Kaena Ridge, we anticipated that nonlinear interactions such as PSI would be highly localized and intermittent. The *FLIP* record, with its significantly broader depth–time coverage than available to previous studies, provides unprecedented spectral resolution and also allows us to examine in detail the vertical

structure and time variability of PSI near the tidal generation site.

We begin by introducing the HOME Nearfield data and identifying possible PSI triads. Resonant interaction theory is briefly reviewed, and we develop an expression for nonlinear energy transfers in the Nearfield setting. Bispectral methods are used to map the energy transfer terms in (bi)frequency space and test the significance of possible interactions between the semidiurnal tide and near-diurnal daughter waves. A novel prefiltering technique, which separates subharmonic wave energy into up-going and down-going components, is used to test the prediction of resonant theory that the interacting PSI daughter waves will exhibit opposite signs of vertical propagation. Returning to the depth–time domain, we map the PSI interaction terms as they evolve in time and space and attempt to form a time-averaged profile of the energy transfer rate. In conclusion, we discuss the likely relevance of PSI to local turbulent mixing and long range tidal propagation.

2. Resonant PSI

To motivate our discussion of PSI-like interactions in the HOME Nearfield, it is useful to first revisit the source of nonlinear energy transfers in the equations of motion. For the inviscid Boussinesq system

$$\frac{\partial \mathbf{u}}{\partial t} + \mathbf{u}\cdot\nabla\mathbf{u} + \mathbf{f}\times\mathbf{u} = -\nabla p'/\rho_0 - \rho'\mathbf{g}/\rho_0 \quad \text{and} \tag{3}$$

$$\nabla\cdot\mathbf{u} = 0, \tag{4}$$

where $\mathbf{u}$ is the vector velocity, p' and ρ' are perturbation pressure and density, and ρ_0 is the background density, linearized solutions exist in the form of plane internal waves, with velocity, pressure, and density expressed in terms of Fourier coefficients

$$\mathbf{u} = \hat{\mathbf{u}}e^{i(\mathbf{k}\cdot\mathbf{x}-\omega t)} + \hat{\mathbf{u}}^* e^{-i(\mathbf{k}\cdot\mathbf{x}-\omega t)} \quad \text{and} \tag{5}$$

$$p' = \hat{p}e^{i(\mathbf{k}\cdot\mathbf{x}-\omega t)} + \text{c.c.}, \quad \rho' = \hat{\rho}e^{i(\mathbf{k}\cdot\mathbf{x}-\omega t)} + \text{c.c.}, \tag{6}$$

where the symbols c.c. denote complex conjugates. The wave vector and frequency $(\mathbf{k}, \omega)$ satisfy the linear dispersion relationship

$$\omega^2(\mathbf{k}) = \frac{f^2m^2 + N^2(k^2+l^2)}{k^2+l^2+m^2}, \quad \mathbf{k} = (k,l,m). \tag{7}$$

In the weakly nonlinear formulation, the linear waves are allowed to interact slowly through the quadratic term $\mathbf{u}\cdot\nabla\mathbf{u}$ in (3). Consider a wave field containing three distinct wave vectors and frequencies, $[(\mathbf{k}_1, \omega_1), (\mathbf{k}_2, \omega_2), (\mathbf{k}_3, \omega_3)]$, with total velocity

$$\mathbf{u} = \mathbf{u}_1 + \mathbf{u}_2 + \mathbf{u}_3. \tag{8}$$

The momentum equation for a single wave, for example, $\mathbf{u}_1$, can be found by substituting (8) into (3) and using the fact that each wave is an independent solution to the linearized system

$$\frac{\partial \mathbf{u}_1}{\partial t} + (\mathbf{u}_1+\mathbf{u}_2+\mathbf{u}_3)\cdot\nabla(\mathbf{u}_1+\mathbf{u}_2+\mathbf{u}_3) + \mathbf{f}\times\mathbf{u}_1 = -\nabla p_1/\rho_0 - \rho_1\mathbf{g}/\rho_0. \tag{9}$$

If the waves satisfy (1), then the terms $\mathbf{u}_2\cdot\nabla\mathbf{u}_3$ and $\mathbf{u}_3\cdot\nabla\mathbf{u}_2$ drive $\mathbf{u}_1$ resonantly, as seen in the energy equation that is obtained by taking the scalar product of $\mathbf{u}_1$ with (9) and averaging $\langle\cdot\rangle$ over space and time scales, which are large compared to the wave scales,

$$\left\langle \frac{\partial}{\partial t}\frac{1}{2}\|\mathbf{u}_1\|^2 \right\rangle + \langle \mathbf{u}_1\cdot(\mathbf{u}_1+\mathbf{u}_2+\mathbf{u}_3)\cdot\nabla(\mathbf{u}_1+\mathbf{u}_2+\mathbf{u}_3)\rangle = -\left\langle \frac{1}{\rho_0}\nabla\cdot(p_1\mathbf{u}_1)\right\rangle - \left\langle \frac{1}{\rho_0}g\rho_1 w_1\right\rangle. \tag{10}$$

In the triple product term which appears in (10), only the terms that contain zero frequency and wavenumber, which are the products of $\mathbf{u}_1$ with resonant terms, have nonzero averages over time and space; the remaining oscillatory terms disappear,

$$\langle \mathbf{u}_1\cdot(\mathbf{u}_1+\mathbf{u}_2+\mathbf{u}_3)\cdot\nabla(\mathbf{u}_1+\mathbf{u}_2+\mathbf{u}_3)\rangle = \langle \mathbf{u}_1\cdot(\mathbf{u}_2\cdot\nabla\mathbf{u}_3 + \mathbf{u}_3\cdot\nabla\mathbf{u}_2)\rangle. \tag{11}$$

Meanwhile, the first and last terms in (10) are the time rates of change of kinetic and potential energy density, E_k and E_P, which we can combine into a total rate of change of energy associated with $\mathbf{u}_1$,

$$\left\langle \frac{\partial}{\partial t}\frac{1}{2}\|\mathbf{u}_1\|^2 \right\rangle + \left\langle \frac{1}{\rho_0}g\rho_1 w_1\right\rangle = \frac{\partial E_k}{\partial t} + \frac{\partial E_p}{\partial t} = \frac{\partial E_1}{\partial t}. \tag{12}$$

Finally, the pressure–velocity term represents the divergence of energy flux, $\nabla\cdot\mathbf{F}$, which is equal to the group velocity $\mathbf{c}_g$ times wave energy density

$$\left\langle \frac{1}{\rho_0}\nabla\cdot p_1\mathbf{u}_1\right\rangle = \nabla\cdot\mathbf{F} = \nabla\cdot\mathbf{c}_g E_1. \tag{13}$$

Using (11)–(13), we can rewrite (10) as

$$\frac{\partial E_1}{\partial t} + \nabla\cdot\mathbf{c}_g E_1 = \mathcal{G} \quad \text{and} \tag{14}$$

$$\mathcal{G} = -\langle \mathbf{u}_1\cdot(\mathbf{u}_2\cdot\nabla\mathbf{u}_3 + \mathbf{u}_3\cdot\nabla\mathbf{u}_2)\rangle, \tag{15}$$

which expresses a balance between resonant energy transfer and wave radiation.

PSI of the internal tide

We now specifically consider a PSI-like resonant triad, where $(\mathbf{k}, \omega) = (\mathbf{k}_3, \omega_3)$ is associated with a low-mode semidiurnal tide whose velocity we denoted by $\mathbf{U} = \mathbf{u}_3$. The pair of waves at $(\mathbf{k}_1, \omega_1)$, $(\mathbf{k}_2, \omega_2)$ represent subharmonics of the tide.

The PSI source term becomes

$$\mathcal{G} = -\langle \mathbf{u}_1 \cdot (\mathbf{u}_2 \cdot \nabla \mathbf{U}) \rangle - \langle \mathbf{u}_1 \cdot (\mathbf{U} \cdot \nabla \mathbf{u}_2) \rangle . \quad (16)$$

Analysis of PSI near the critical latitude (MacKinnon and Winters 2005; Young et al. 2008) suggests that the term $\langle \mathbf{u}_1 \cdot (\mathbf{u}_2 \cdot \nabla \mathbf{U}) \rangle$, which is affected by tidal gradients, is the primary driver of PSI rather than the term $\langle \mathbf{u}_1 \cdot (\mathbf{U} \cdot \nabla \mathbf{u}_2) \rangle$, which is affected by tidal advection. Equatorward of the critical latitude, the subharmonic waves can have distinct, significantly superinertial frequencies. We therefore depart from Young et al. (2008)'s framework, which contains for a single near-inertial disturbance, and consider energy transfers to *pairs* of *superinertial* waves. The subharmonics are assumed to be weakly nonlinear waves in the Lagrangian coordinate frame

$$\mathbf{x}'(t) = (x', y', z'), \quad (17)$$

which follows tidal motions $\mathbf{U}(\mathbf{x}', t)$. The Eulerian and Lagrangian coordinates are related through

$$\mathbf{x} = \mathbf{x}' + \boldsymbol{\xi}(\mathbf{x}', t), \quad (18)$$

where $\boldsymbol{\xi}(\mathbf{x}', t)$ are the Eulerian particle displacements

$$\boldsymbol{\xi}(\mathbf{x}', t) = [\xi(\mathbf{x}', t), \zeta(\mathbf{x}', t), \eta(\mathbf{x}', t)] = \int_0^t \mathbf{U}(\mathbf{x}', t')\, dt' . \quad (19)$$

Let symbols for other quantities in tide-following coordinates also be denoted by primes. The local gradient of the tide is

$$\nabla \mathbf{U}' = \nabla \mathbf{U}(\mathbf{x}'), \quad (20)$$

but the background velocity disappears

$$\mathbf{U}' = \mathbf{U}(\mathbf{x}') = 0. \quad (21)$$

Thus, in the tide-following frame, the energy Eq. (14) becomes

$$\frac{\partial E_1'}{\partial t} + \nabla \cdot \mathbf{c}_g' E_1' = \mathcal{G}' \quad \text{and} \quad (22)$$

$$\mathcal{G}' = -\langle \mathbf{u}_1' \cdot (\mathbf{u}_2' \cdot \nabla \mathbf{U}') \rangle . \quad (23)$$

If $\mathbf{u}_1$ are $\mathbf{u}_2$ are superinertial, then they can have nonnegligible vertical velocities. Writing $\mathcal{G}'$ in terms of Fourier coefficients (5) and dropping the primes, we keep both the horizontal and vertical gradient terms

$$\mathcal{G}' = -\langle \mathbf{u}_1' \cdot (\mathbf{u}_2' \cdot \nabla \mathbf{U}') \rangle = -\hat{\mathbf{u}}_1 \cdot (-i\mathbf{k} \cdot \hat{\mathbf{u}}_2) \hat{\mathbf{U}}^* + \text{c.c.} \quad (24)$$

$$= (ik\hat{u}_2 + il\hat{v}_2 + im\hat{w}_2)(\hat{\mathbf{u}}_1 \cdot \hat{\mathbf{U}}^*) + \text{c.c.} \quad (25)$$

$$= (ik\hat{u}_2 + il\hat{v}_2 + im\hat{w}_2)(\hat{u}_1 \hat{U}^* + \hat{v}_1 \hat{V}^* + \hat{w}_1 \hat{W}^*) + \text{c.c.} \quad (26)$$

Assuming that $(\mathbf{k}_1, \mathbf{k}_2, \mathbf{k})$ lie in a vertical plane, we can orient the horizontal coordinate axes so that the x axis lies in the same plane. Then the internal wave polarization relations (Gill 1982) give

$$v = -\frac{if}{\omega}(\hat{u} - \hat{u}^*), \quad w = -\frac{k}{m}(\hat{u} + \hat{u}^*), \quad (27)$$

and we can express $\mathcal{G}'$ in terms of its u components

$$\mathcal{G}' = (ik)\hat{u}_1 \hat{u}_2 \hat{U}^* \left(1 - \frac{m}{k}\frac{k_2}{m_2}\right)\left(1 + \frac{f}{\omega_1}\frac{f}{\omega} + \frac{k_1}{m_1}\frac{k}{m}\right) + \text{c.c.} \quad (28)$$

The aspect ratios α for each wave are set through the dispersion relation (7), in the form

$$\alpha^2 = \frac{k^2}{m^2} = \pm\left(\frac{\omega^2 - f^2}{N^2 - \omega^2}\right) \approx \left(\frac{\omega^2 - f^2}{N^2}\right) \quad \text{for} \quad \omega \ll N, \quad (29)$$

so that the difference term in (28) is

$$\left(1 - \frac{m}{k}\frac{k_2}{m_2}\right) = \left(1 - \frac{\alpha_2}{\alpha}\right) \approx \left[1 \mp \left(\frac{\omega_2^2 - f^2}{\omega^2 - f^2}\right)^{1/2}\right], \quad (30)$$

where the sign taken is opposite that of α_2/α. From (29) it also follows that $k/m \ll f/\omega$, hence $(k_1/m_1)(k/m) \ll (f/\omega_1)(f/\omega)$, and the sum term in (28) is approximately

$$\left(1 + \frac{f}{\omega_1}\frac{f}{\omega} + \frac{k_1}{m_1}\frac{k}{m}\right) \approx \left(1 + \frac{f}{\omega_1}\frac{f}{\omega}\right). \quad (31)$$

Combining (28)–(31), the PSI source term becomes

$$\mathcal{G}' \approx (ik)\hat{u}_1 \hat{u}_2 \hat{U}^* \left(1 + \frac{f^2}{\omega_1 \omega}\right)\left[1 \mp \left(\frac{\omega_2^2 - f^2}{\omega^2 - f^2}\right)^{1/2}\right] + (f/\omega_1). \quad (32)$$

Near Kaena Ridge (21.68°N), where $f = 1/32.4\,\mathrm{h}$ and $\omega_1 \approx M_2/2 \approx (1/12.42\,\mathrm{h})/2 \approx 1.3f$,

$$\mathcal{G}' \approx (1.7)(ik)\hat{u}_1\hat{u}_2\hat{U}^* + \text{c.c.} \quad \text{for} \quad \frac{\alpha_2}{\alpha} < 0. \quad (33)$$

In the limit of near-inertial PSI, where $\omega_1 \approx \omega_2 \to f$ and hence $\omega \to 2f$,

$$\mathcal{G}' \to \frac{3}{2}(ik)\hat{u}_1\hat{u}_2\hat{U}^* + \text{c.c.}, \quad (34)$$

recovering the expression found in MacKinnon and Winters (2005) and MacKinnon et al. (2012).

In each of the expressions above, the energy transfer rate is determined by the relative amplitudes and phases of the triad members up to a constant k, the horizontal wavenumber of the primary wave. For a realistic ocean, in which many triads can be interacting simultaneously, it is useful to form a map of the triple product $\hat{u}_1\hat{u}_2\hat{U}^*$ across all possible resonant triads. After introducing the data in the following section, we will return to map the triad interactions using bispectral methods.

3. Observations

During the fall of 2002 HOME Nearfield component, the Research Platform *FLIP* was moored in Kauai Channel in 1100 m of water, on the southwest slope of Kaena Ridge, Hawaii (21.68°N, 158.63°W) (Fig. 1). The objective of the cruise was to observe internal wave generation, fluxes, and dissipation close to the ridge. Kaena Ridge was identified during the HOME survey as a site of particularly intense barotropic-to-baroclinic tidal conversion (Egbert and Ray 2001; St. Laurent and Garrett 2002; Rudnick et al. 2003). *FLIP*'s profiling column intersected a M_2 tidal beam, which emanated upward from the northeast edge of the ridge, propagating across from the ridge toward the south–southwest and carrying an estimated depth-integrated energy flux of $O(1\ \mathrm{KW\ m^{-1}})$ normal to the ridge crest (Rainville and Pinkel 2006a).

During the 35-day data collection period, conductivity and salinity profiles were recorded by tandem SeaBird SBE11 CTDs once every 4 min, covering 15–800-m depths and achieving a vertical resolution of approximately 2 m. The Deep-8, a combination up–down-looking Doppler sonar transmitting repeat-sequence coded pulses (Pinkel and Smith 1992), was deployed on a cable at a depth of 400 m and measured horizontal velocities with a 4-m vertical resolution. Baroclinic horizontal velocities were estimated by subtracting Ocean Topography Experiment (TOPEX)/Poseidon Cross-Over Global Inverse Solution, Version 5.1 (TPO.5.1) model barotropic velocities (Egbert 1997; Egbert and Erofeeva 2002) from the total

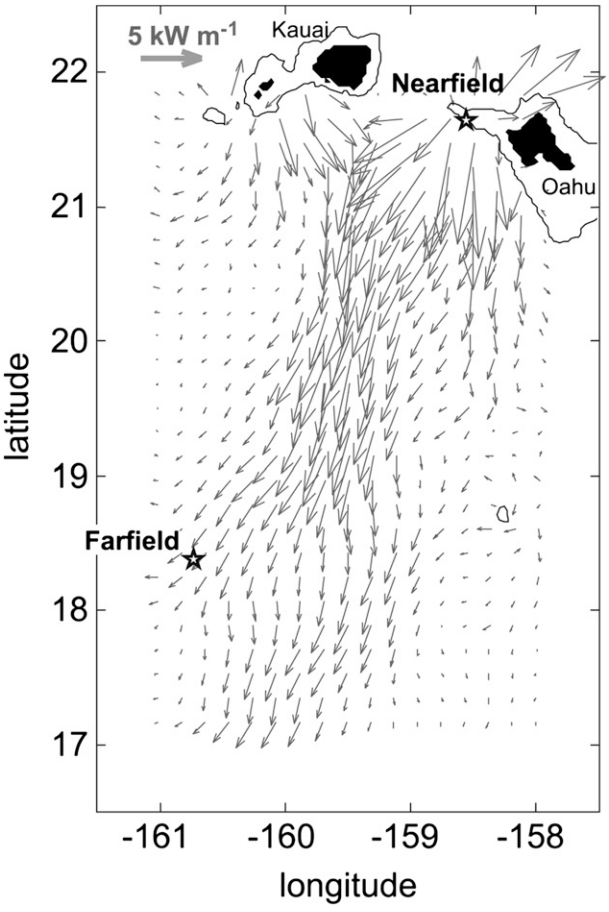

FIG. 1. Deployment of the Research Platform *FLIP* in 2001/02 (Rainville and Pinkel 2006a). As part of the Hawaii Ocean Mixing Experiment, *FLIP* was moored at two locations near Kaena Ridge, Hawaii. During the 2002 Farfield component, the measurement location was approximately 430 km to the southwest of the ridge crest, in the approximate path of an M_2 tidal beam (model fluxes are shown by the arrows). The 2002 Nearfield component placed *FLIP* on the shoulder of Kaena Ridge in approximately 1100 m of water, in a location intersecting the southward-propagating ray emanating from the northern ridge crest.

velocities measured by the Deep-8. Vertical velocities were inferred from isopycnal displacements, which were derived from the CTD data. Figure 2 shows a diagram of *FLIP* and its instruments. For a detailed discussion of the instruments and deployment site, see Rainville and Pinkel (2006a).

Semi-Lagrangian coordinates are used throughout the presentation and analysis of the data. The mutual advection of finite amplitude waves in Eulerian coordinates is a nonlinear process that is reversible, that is, not associated with a net energy transfer. However, spectral estimates in the Eulerian frame are susceptible to Doppler spreading, particularly that of high-vertical-wavenumber motions by tidal heaving (Rainville and Pinkel 2006a;

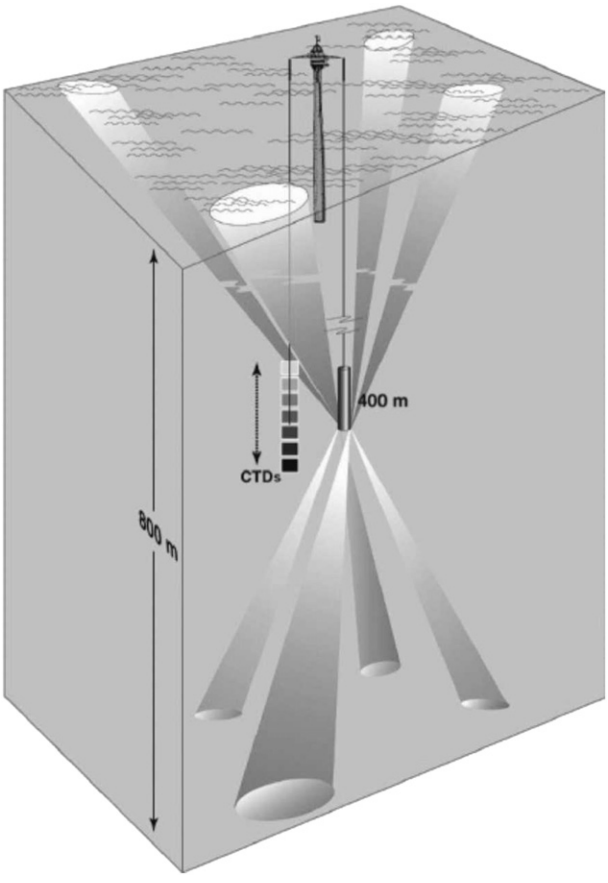

FIG. 2. Schematic of R/P *FLIP* instrumentation during HOME, 2001/02. Tandem Seabird SBE11 CTDs profiled down to approximately 800 m once every 4 m with approximately 2-m resolution. The Deep-8 Doppler sonar recorded horizontal velocities with approximately 4-m vertical resolution. Vertical velocities were inferred from the motion of isopycnals as measured by the CTDs. More than 11 000 profiles were collected during the Nearfield and more than 9000 during the Farfield.

Pinkel 2008). In the semi-Lagrangian frame, the vertical coordinate is fixed to isopycnals, thereby minimizing advective distortion. Reference isopycnals are based upon the cruise-averaged density profile $\rho_0(z)$ and chosen with a two-meter mean separation. The reference depths are Wentzel-Kramers-Brillouin (WKB)-stretched (Gill 1982)

$$z_{\mathrm{wkb}}(z) = \frac{1}{N_0}\int_0^z N(z)\,dz, \tag{35}$$

to correct for refractive effects because of the depth dependence of the stratification. A constant base stratification N_0 is chosen to keep the profiling range the same before and after rescaling. Velocities (u, v, w) and isopycnal displacements η are also scaled according to linear theory (Gill 1982)

$$\eta = \eta_0\frac{N}{N_0}, \quad w = w_0\sqrt{\frac{N}{N_0}}, \quad (u,v) = (u_0,v_0)\sqrt{\frac{N_0}{N}}. \tag{36}$$

The horizontal axes are oriented so that u is pointed across ridge and away, at $-120°$ relative to east, matching the direction of semidiurnal energy flux observed by Rainville and Pinkel (2006a). Following a right-handed convention, v is at $-30°$ to east.

a. Depth–time maps

WKB-scaled isopycnal displacements η, presented in Fig. 3, are predominantly large-scale motions associated with the semidiurnal tide. The scale height of the waves is comparable to the entire profiling depth. A slight backward slant to the wave crests, visible below about 200 m, shows downward phase propagation and hence upward energy propagation. The sign of propagation is consistent with tidal generation at the ridge and upward energy flux (Rainville and Pinkel 2006a). A fortnightly cycle is visible with spring tides arriving around days 263–264 and 277–278. At peak spring tide, displacements below 500-m depth reach 70 m, corresponding to a 100-m true displacement. A brief interruption in data collection can be seen in the velocities on day 280, after the 8099th profile, when a CTD collided with the Deep-8. Afterward, the coverage of the CTD was reduced to a maximum depth of ≈710 m.

Horizontal velocities (u, v), shown in Fig. 4 show contributions from inertial–diurnal, semidiurnal, and higher frequencies at a mix of scales. Here, as in the displacements, a fortnightly cycle is apparent, but peak velocities are seen near days 271 and 281, a few days after the peak displacements. Maximum velocities approach 50 cm s^{-1} near 200-m depth. Persistent velocity artifacts around depths 150–156, 412–424, and 526–552 m were caused by boundary reflections and the transition from upward-looking to downward-looking modes of the Deep-8. While the artifacts were originally confined to fixed depth ranges in Eulerian coordinates, the change to semi-Lagrangian coordinates spreads the disruptions over an additional 10–20 m in the vertical. Velocities are interpolated for visual presentation, but the affected ranges are discarded whenever depth averages are subsequently computed.

In semi-Lagrangian coordinates, the vertical separation of reference isopycnals is time dependent, so we estimate shears as centered differences of velocity divided by the instantaneous separation of isopycnals (with mean separation 4 m). Shear amplitudes are found to vary more closely as N than the $N^{3/2}$ predicted by linear theory, so that the shears are normalized by

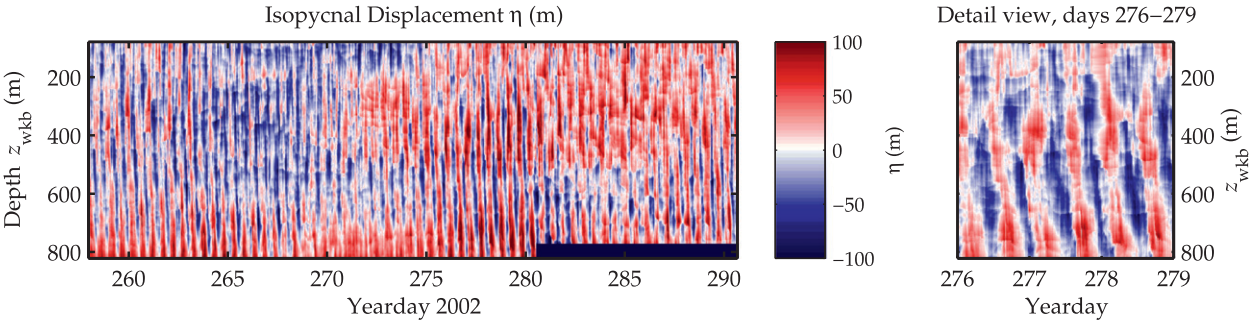

FIG. 3. (left) Isopycnal displacements η for yeardays 260–290 with (right) detailed view for yeardays 276–279. Baroclinic vertical displacements are of order 100 m at depths below 500 m. Long vertical scales dominate the record. Peak spring tides appear around days 265 and 279. The maximum depth of the CTD profiles was reduced to 710 m after day 280.

$$(u_z, v_z) = \left(\frac{N_0}{N}\right)(u_{z0}, v_{z0}). \tag{37}$$

Figure 5 presents the semi-Lagrangian shears (u_z, v_z), which in Fig. 6 are compared with Eulerian versions that are computed as centered differences over fixed depths with 4-m spacing. The vertical shears are weighted toward small-scale motions, relative to the horizontal velocities, and a pattern emerges of waves with 100–150-m wavelength and frequency between inertial and diurnal frequency. As with the velocities, there is a hint of a fortnightly cycle in the shears that lags behind the peak semidiurnal

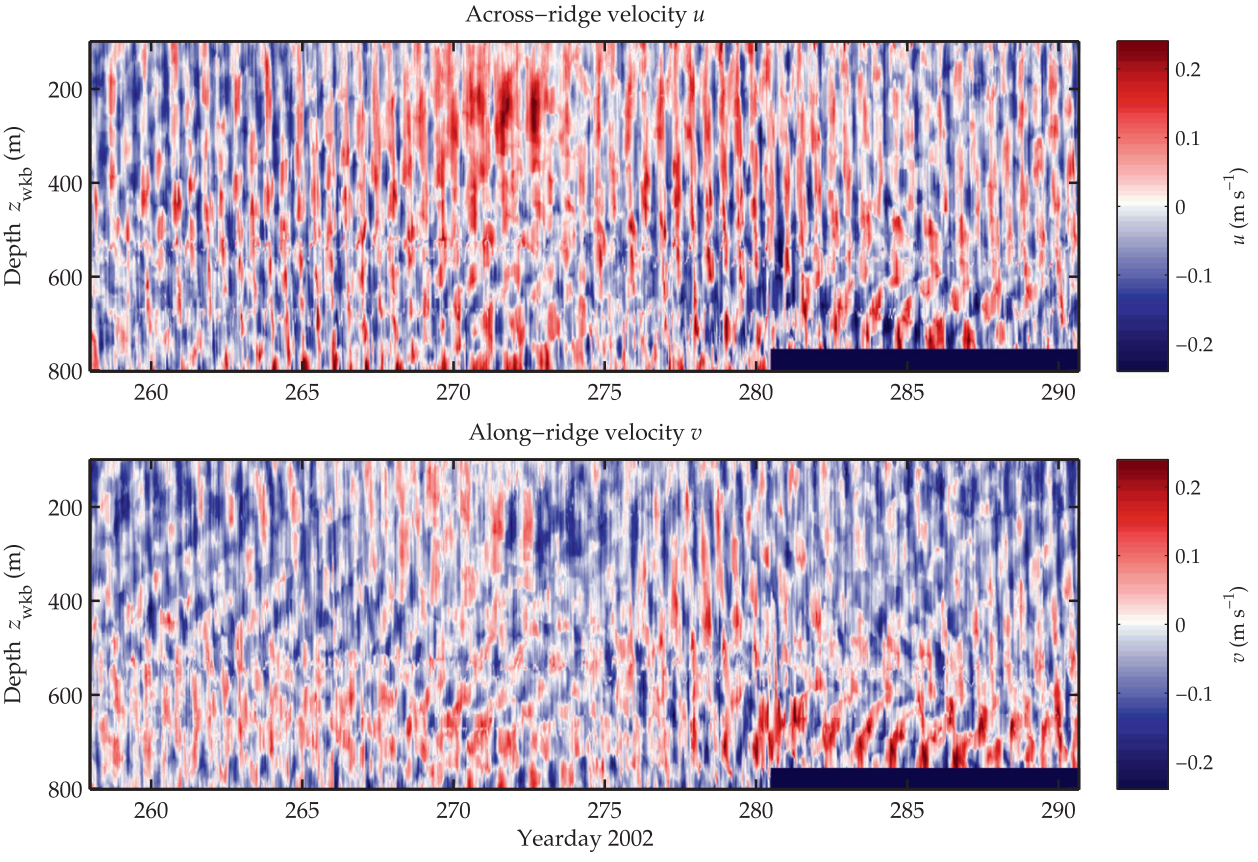

FIG. 4. Velocities (u, v) in semi-Lagrangian coordinates. (top) Across-ridge velocity component u, defined as pointing away, $-120°$ relative to east. (bottom) Along-ridge velocity component v, defined as pointing $-30°$ relative to east. Both u and v contain a superposition of a mix of scales and frequencies including inertial-diurnal, semidiurnal, and higher-frequency motions. The reduced depth of the CTD profiles after day 280 affects the semi-Lagrangian velocities, which depend upon isopycnal depth information.

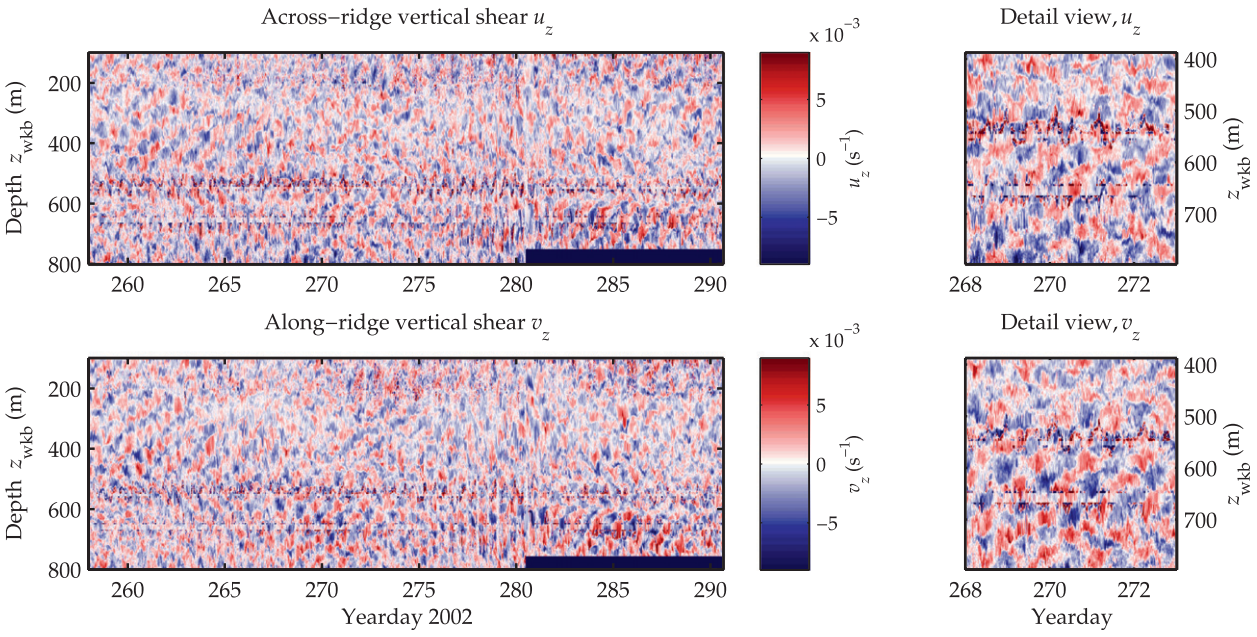

FIG. 5. (left) Vertical shears (u_z, v_z) in semi-Lagrangian coordinates. Shear amplitudes are scaled by N/N_0 and the vertical coordinate is WKB-stretched. Waves with short vertical scales of about 100–150 m and approximately diurnal period are seen propagating both upward and downward, creating an × or chevron-shaped standing wave pattern. (right) Detailed view showing the differences between semi-Lagrangian and Eulerian shears in a region where isopycnals are visibly distorted by the vertical heaving of the semidiurnal tide. A hint of a fornightly cycle can be seen in the variance, which peaks around days 271 and 285, or about 5–7 days after peak spring tides (days 265 and 279).

displacements by a few days. The waves' frequency, spatial scales, and timing are all consistent with PSI subharmonics, which grow in response to the spring tide.

In the Eulerian frame (Fig. 6, bottom), the wave crests are strongly distorted by tidal motions (Fig. 3), which displace isopycnals by a distance comparable to a wavelength of the inertial–diurnal waves. Waves in the semi-Lagrangian frame have a qualitatively more ''linear'' appearance, such that wave crests appear as nearly straight lines when plotted against the WKB-stretched vertical coordinate. Both upward- and downward-propagating waves are present in roughly equal parts, and with the straightened wave crests they combine to form a characteristic chevron or × shape, which is most prominent below 400-m depth. A similar spatial pattern, associated with the opposite-sign propagation of PSI daughter waves, was previously seen in studies of PSI near the M_2 critical latitude, both in numerical simulations (MacKinnon and Winters 2005) and in observations during IWAP (Alford et al. 2007).

b. *Spectral estimates*

Power spectral estimates for the displacements, velocities, and shears are computed by a multitaper method, using a sequence of four prolate spheroidal tapers. Multitaper estimates for these data give a similar result to smoothed periodograms, but are here used because they exhibit slightly less leakage to frequencies away from the main peaks.

Depth–frequency spectra for isopycnal displacements, presented in Fig. 7, confirm that the semidiurnal frequency (M_2 = 1/12.42 h) dominates throughout the water column. A peak in semidiurnal variance is seen near 550-m depth and a second, weaker peak at 360 m. Motions near the subharmonic $M_2/2$ are also visible, with peak variances about an order of magnitude lower than M_2 peak. Depth-averaged displacement spectra (Fig. 8) show that the subharmonic frequency is distinct from the local inertial frequency (f = 1/32.7 h). A series of weaker interaction lines are also visible at the frequencies $M_2 + M_2/2, 2M_2, \ldots$.

The vertical strain rate η_z measures the dilation of layers between isopycnal surfaces. While some strain variance is visible in the spectra (Fig. 7, bottom), around $M_2/2$, the energetic M_2 motions associated with the low-mode tide create very little strain.

Rotary spectral estimates of velocity and shear are formed from the complex quantities

$$\mathcal{U} = u + iv, \quad \mathcal{U}_z = u_z + iv_z, \tag{38}$$

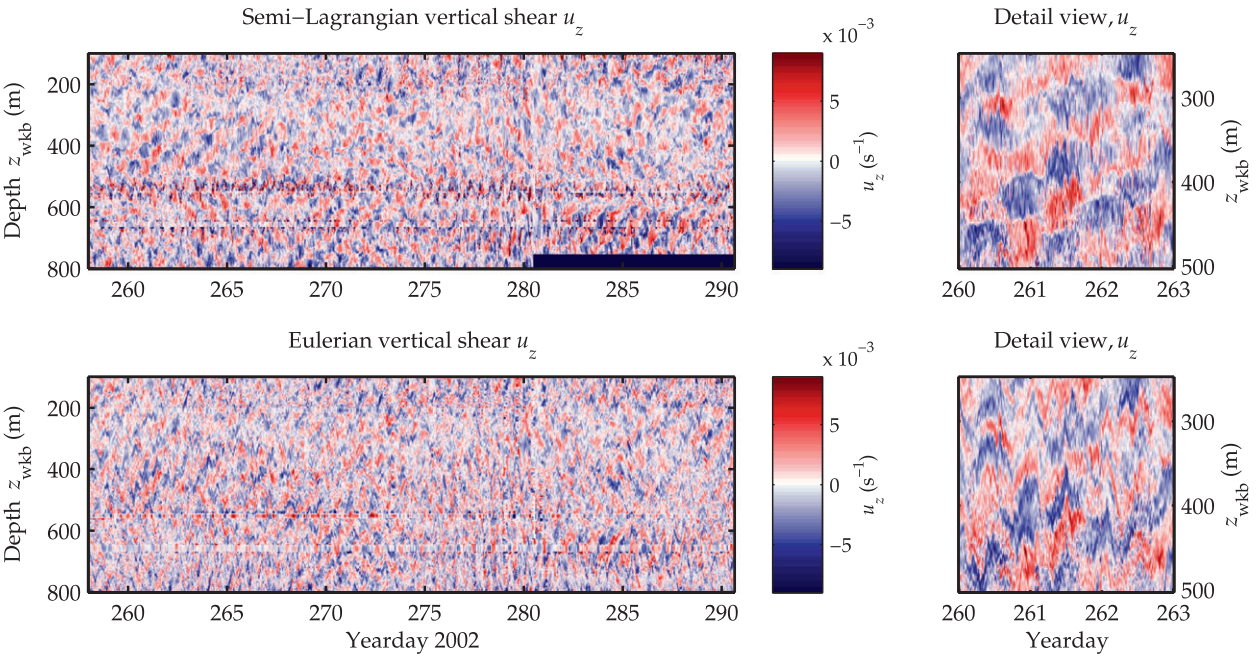

FIG. 6. Across-ridge vertical shear u_z in semi-Lagrangian and Eulerian coordinates. As in Fig. 5, but showing a comparison of across-ridge shear in different coordinate frames. Shear amplitudes are scaled by N/N_0 and the vertical coordinate is WKB-stretched. The detail view highlights the differences between semi-Lagrangian and Eulerian shears. Wave crests in the Eulerian frame are visibly distorted by the vertical heaving of the semidiurnal tide. In the semi-Lagrangian frame, which follows isopycnals as they move vertically with the tide, waves are restored to a more linear appearance and exhibit relatively straight wave crests.

which are scaled using (36) and (37). Taking Fourier transforms decomposes the contributions at each frequency ω into sums, for example,

$$\mathcal{U} = \hat{\mathcal{U}} e^{-i\omega t} + \hat{\mathcal{U}}_* e^{i\omega t}, \tag{39}$$

of motions which rotate in time in the anticyclonic and cyclonic directions, respectively. The new symbol $\hat{\mathcal{U}}_*(\omega) = \hat{\mathcal{U}}(-\omega)$ emphasizes that $\hat{\mathcal{U}}$ is not conjugate-symmetric, that is, $\hat{\mathcal{U}}_* \neq \hat{\mathcal{U}}^*$.

The relationship between $(\hat{\mathcal{U}}, \hat{\mathcal{U}}_*)$ and the Fourier coefficients $(\hat{u}, \hat{v})$ associated with the linear components of motion in (38), is found by substituting (5) into (39),

$$\hat{\mathcal{U}} e^{-i\omega t} + \hat{\mathcal{U}}_* e^{i\omega t} = (\hat{u} e^{-i\omega t} + \hat{u}^* e^{i\omega t}) + i(\hat{v} e^{-i\omega t} + \hat{v}^* e^{i\omega t}), \tag{40}$$

and using the polarization relations (27),

$$= (\hat{u} e^{-i\omega t} + \hat{u}^* e^{i\omega t}) + i\left(-\frac{if}{\omega}\right)(\hat{u} e^{-i\omega t} - \hat{u}^* e^{i\omega t}) \tag{41}$$

$$= \hat{u}\left(1 + \frac{f}{\omega}\right) e^{-i\omega t} + \hat{u}\left(1 - \frac{f}{\omega}\right) e^{i\omega t}. \tag{42}$$

Equating coefficients we obtain

$$\hat{\mathcal{U}} = \hat{u}\left(1 + \frac{f}{\omega}\right), \quad \hat{\mathcal{U}}_* = \hat{u}^*\left(1 - \frac{f}{\omega}\right), \tag{43}$$

which gives a ratio of anticyclonic to cyclonic motions

$$\frac{|\hat{\mathcal{U}}|}{|\hat{\mathcal{U}}_*|} = \frac{\omega + f}{\omega - f}. \tag{44}$$

Waves with frequency ω close to f have nearly all of their motion in the anticyclonic component $\hat{\mathcal{U}} e^{-i\omega t}$. For $\omega \approx M_2/2 \approx 1.3\, f$, the ratio is $|\hat{\mathcal{U}}|/|\hat{\mathcal{U}}_*| \approx 7.7/1$, for a ratio of variances $|\hat{\mathcal{U}}|^2/|\hat{\mathcal{U}}_*|^2 \approx 60/1$. By contrast, variance associated with uncorrelated noise in u or v is spread equally between the anticyclonic and cyclonic components. The expected bias toward anticyclonic motions serves as a consistency check for internal waves in the following spectral estimates for $\mathcal{U}$.

Velocity depth–frequency spectra are presented in Fig. 9, in both the semi-Lagrangian (top) and Eulerian (bottom) coordinate systems. In both, the largest velocity variances appear in a broad band spanning both the inertial and diurnal frequencies and that we hereafter refer to as the inertial–diurnal or f–D_1 band. Peak f–D_1 variance is concentrated toward f between approximately 300- and 550-m depth and toward D_1 above and below those depths. As expected from (43),

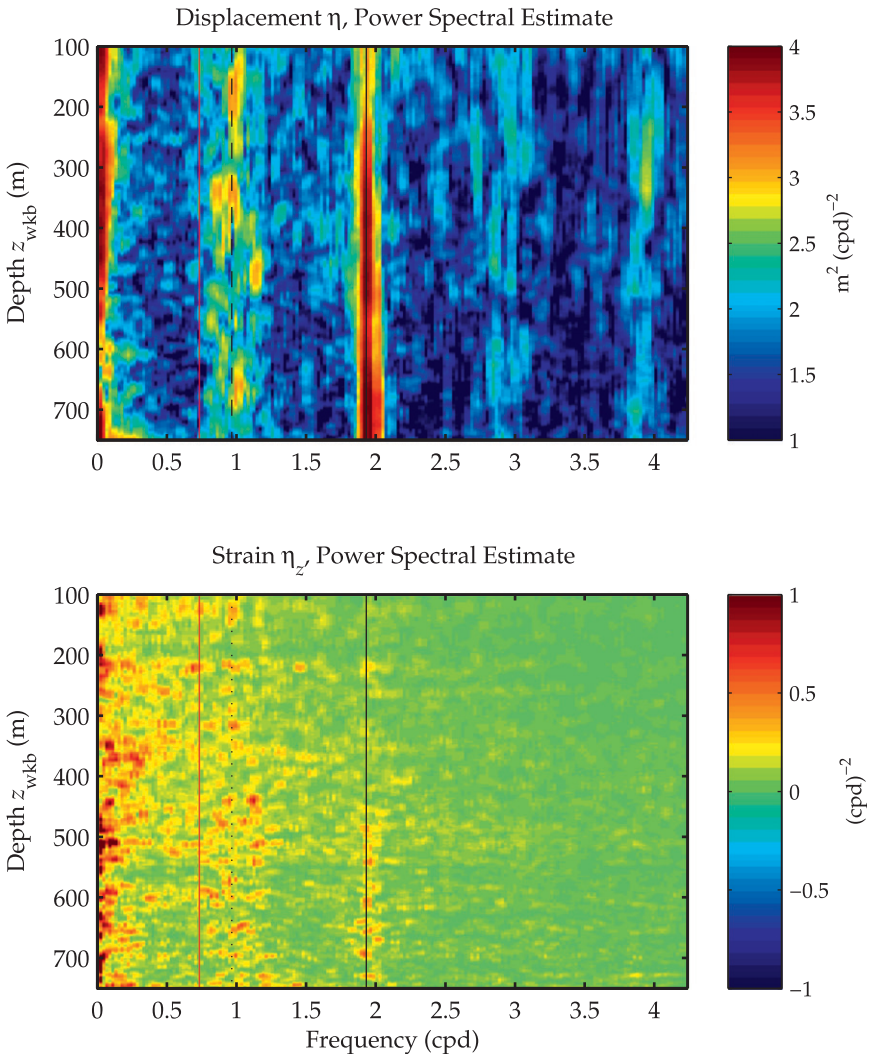

FIG. 7. Power spectral estimate of (top) isopycnal displacement η and (bottom) vertical strain η_z. In (top) semidiurnal motions at M_2 frequency are accompanied by a subharmonic at $M_2/2$ that is clearly distinct from the local inertial frequency f. In (bottom) some variance is visible around $M_2/2$, but as with shear, the energetic motions of the low-mode M_2 tide are associated with relatively little strain.

near-inertial variance is contained almost entirely in the anticyclonic half-plane, near f. Most of the remaining f–D_1 variance is also anticyclonic. Using (43), the ratio of anticyclonic to cyclonic variance for waves of frequency $D_1 = 1$ cpd $\approx 2.7f$ is predicted to be

$$\frac{|\hat{\mathcal{U}}|^2}{|\hat{\mathcal{U}}_*|^2} = \left(\frac{\omega + f}{\omega - f}\right)^2 > \frac{40}{1}. \tag{45}$$

Cyclonic variance between $-M_2/2$ and $-(M_2 - f)$ is visible in the Eulerian spectra but nearly absent in the semi-Lagrangian spectra. This signal may be associated with the Doppler shifting of near-inertial waves by the semidiurnal tide. Interaction lines can also be seen at multiples $nM_2/2$ in the Eulerian spectra.

For motions near the semidiurnal frequency $\omega = M_2 \approx 2.6f$, (43) predicts

$$\frac{|\hat{\mathcal{U}}|^2}{|\hat{\mathcal{U}}_*|^2} = \left(\frac{\omega + f}{\omega - f}\right)^2 \approx \frac{6}{1}. \tag{46}$$

However, the velocity spectra show a depth dependence that is not explained by simple plane wave polarization relationships. Anticyclonic semidiurnal variance is evident across all depths, but between 450 and 700 m, the variance becomes predominantly cyclonic.

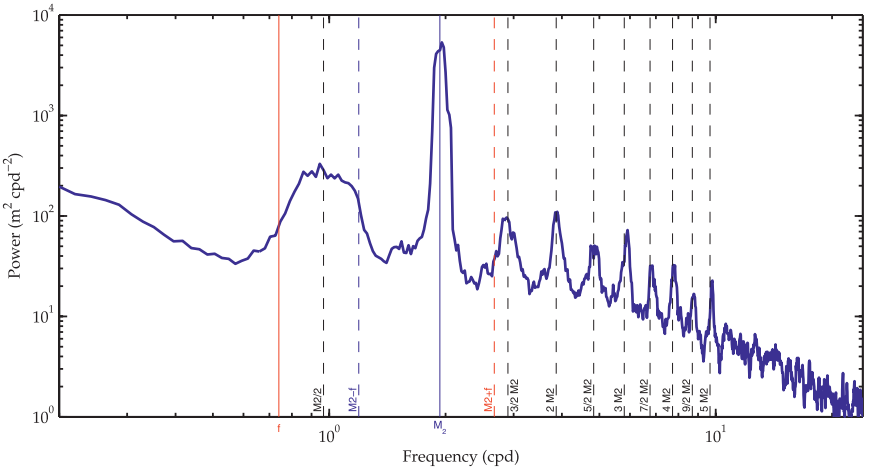

FIG. 8. Depth-averaged power spectral estimates of isopycnal displacement. The M_2 semidiurnal peak dominates the spectrum. The $M_2/2$ subharmonic is prominent and clearly distinct from both the local inertial frequency f and Doppler-shifted frequency $M_2 - f$. A series of harmonics are also visible at $nM_2/2, n = 3, 4, \ldots$.

Shear spectra, shown in Fig. 10, emphasize variance in the f–D_1 band, particularly in the lower depths at frequencies near f. Notably, very little shear variance is evident near the semidiurnal frequency. The wider extent of the data scars in the semi-Lagrangian shear spectrum is clearly visible, as is the presence of additional Doppler-shifted near-inertial ridges in the Eulerian spectrum.

Depth-averaged velocity and shear spectra, shown in Fig. 11, allow comparison of the semi-Lagrangian and Eulerian spectra over a wider range of frequencies. Anticyclonic ($\omega < 0$) variances are indicated in red and cyclonic ($\omega > 0$) in blue. Velocity spectra (top) display anticyclonic/cyclonic velocity ratios, which are generally consistent with (43); nearly all the near-inertial variance is associated with anticyclonic motions. The semi-Lagrangian (thick lines) and Eulerian (thin lines) spectra show approximately equal variances near the semidiurnal frequency $\pm M_2$. The semi-Lagrangian spectra are less susceptible to Doppler shifting of variance away from the near-inertial peak and retain more variance near $-f$ (anticyclonic, red), while the Eulerian spectra contain systematically larger variances away from $\pm M_2$ and $-f$. In particular, the variance at $(M_2 - f)$ is 40%–60% larger in the Eulerian and completely obscures the subharmonic peak at $+M_2/2$.

Nearly all the shear variance (bottom) in both coordinate frames is contained in the f–D_1 band. As in the velocity spectra, there are significant differences in the amount of variance contained in the near-inertial peak. The Eulerian spectra also contain a sharp cyclonic peak between $M_2/2$ and $(M_2 - f)$, which corresponds to the Doppler shifting artifacts seen in the depth–frequency velocity spectra. As with the velocity spectra, the semi-Lagrangian shear spectra retain significantly more variance near f–D_1, while in the Eulerian frame a significant amount of variance is shifted to the left and right by multiples of M_2. Overall, the differences between the semi-Lagrangian and Eulerian shear spectra are similar to the differences seen in the velocity spectra.

4. Bispectra

While conventional spectra measure the variance associated with individual wave frequencies, bispectra measure nonlinear interactions between triads of waves. Formally, the frequency bispectrum of a random variable X is the function defined over the (bi)frequency domain (Hinich and Clay 1968; Kim and Powers 1979)

$$B_X(\omega_1, \omega_2, \omega_1 + \omega_2) = E[\hat{X}(\omega_1)\hat{X}(\omega_2)\hat{X}_*(\omega_1 + \omega_2)], \tag{47}$$

where the $\hat{X}(\omega_1), \hat{X}(\omega_2)$ are the Fourier coefficients of X at frequencies (ω_1, ω_2), the symbol $\hat{X}_*(\omega_1 + \omega_2) = \hat{X}(-\omega_1 - \omega_2)$ as in the previous section, and $E[\cdot]$ indicates an expected value. The third frequency $\omega_1 + \omega$ is sometimes omitted for conciseness.

In a Gaussian wave field, where any triad of waves has random mutual phases, the bispectrum is identically zero. Conversely, a nonzero bispectral estimate implies (partial) phase locking between the waves. If the random variable X is the u component of velocity, then $B_X = B_u$ is exactly the triple product that appears in the PSI source term (33), and phase locking will be associated with a net energy transfer between triad members.

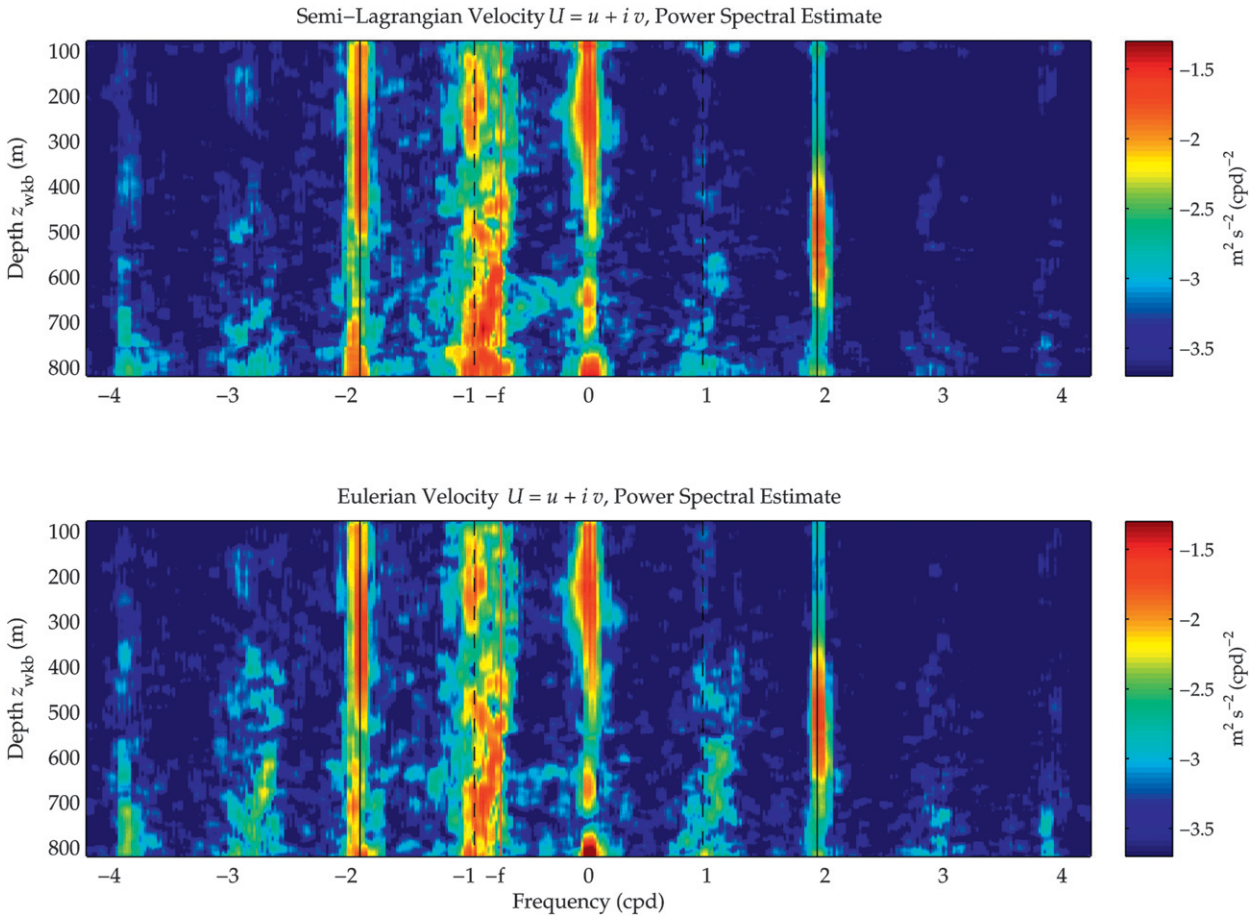

FIG. 9. Two-sided power spectral estimates of complex velocity $\mathcal{U} = (u + iv)$ in (top) Eulerian and (bottom) semi-Lagrangian coordinates. In both coordinate systems, anticyclonic variance is prominent in an "inertial-diurnal" (f–D_1) band that contains both $-f$ and the tidal subharmonic $-M_2/2$ frequency. Near-inertial motions are nearly absent, as expected, on the cyclonic side. The semidiurnal tide appears on both sides at $\pm M_2$. Doppler shifting of the f–D_1 band by multiples of the M_2 tide is evident in the Eulerian frame but nearly absent in the semi-Lagrangian.

A nonzero bispectral value is statistically significant if the bicoherence (Kim and Powers 1979), formed by normalizing the bispectrum, lies outside some confidence interval around zero. We define the (squared) bicoherence following Hinich and Wolinsky (2005)

$$b^2(\omega_1,\omega_2,\omega_1+\omega_2) = \frac{|B(\omega_1,\omega_2)|^2}{E[|\hat{X}(\omega_1)|^2]E[|\hat{X}(\omega_2)|^2]E[|\hat{X}(\omega_1+\omega_2)|^2]}, \tag{48}$$

where $B_X(\omega_1, \omega_2, \omega_1 + \omega_2)$ is normalized by the product of spectral densities at $\omega_1, \omega_2, \omega_1 + \omega_2$. The bicoherence is approximately χ^2 distributed for a large number of degrees of freedom, with confidence intervals around zero bicoherence given by $b^2_{99\%} = 9.2/n_{\mathrm{dof}}$, $b^2_{95\%} = 6.0/n_{\mathrm{dof}}$, and $b^2_{90\%} = 4.6/n_{\mathrm{dof}}$ (Elgar and Guza 1988). The accompanying phase information from (47) is carried in the biphase

$$\phi(\omega_1,\omega_2;\omega_1+\omega_2) = \arctan\left\{\frac{\Im[B(\omega_1,\omega_2,\omega_1+\omega_2)]}{\Re[B(\omega_1,\omega_2,\omega_1+\omega_2)]}\right\}. \tag{49}$$

where $\Re$ and $\Im$ indicate the real and imaginary parts, respectively. In a resonant triad of waves, the biphase is simply the relative phase between nonlinear forcing (created by two of the waves) and the recipient (third) wave.

a. Cross-bispectral estimation of energy transfers

To represent the PSI interaction in bispectral space, we form a cross-bispectrum between the independent variables that appear in the source term (33).

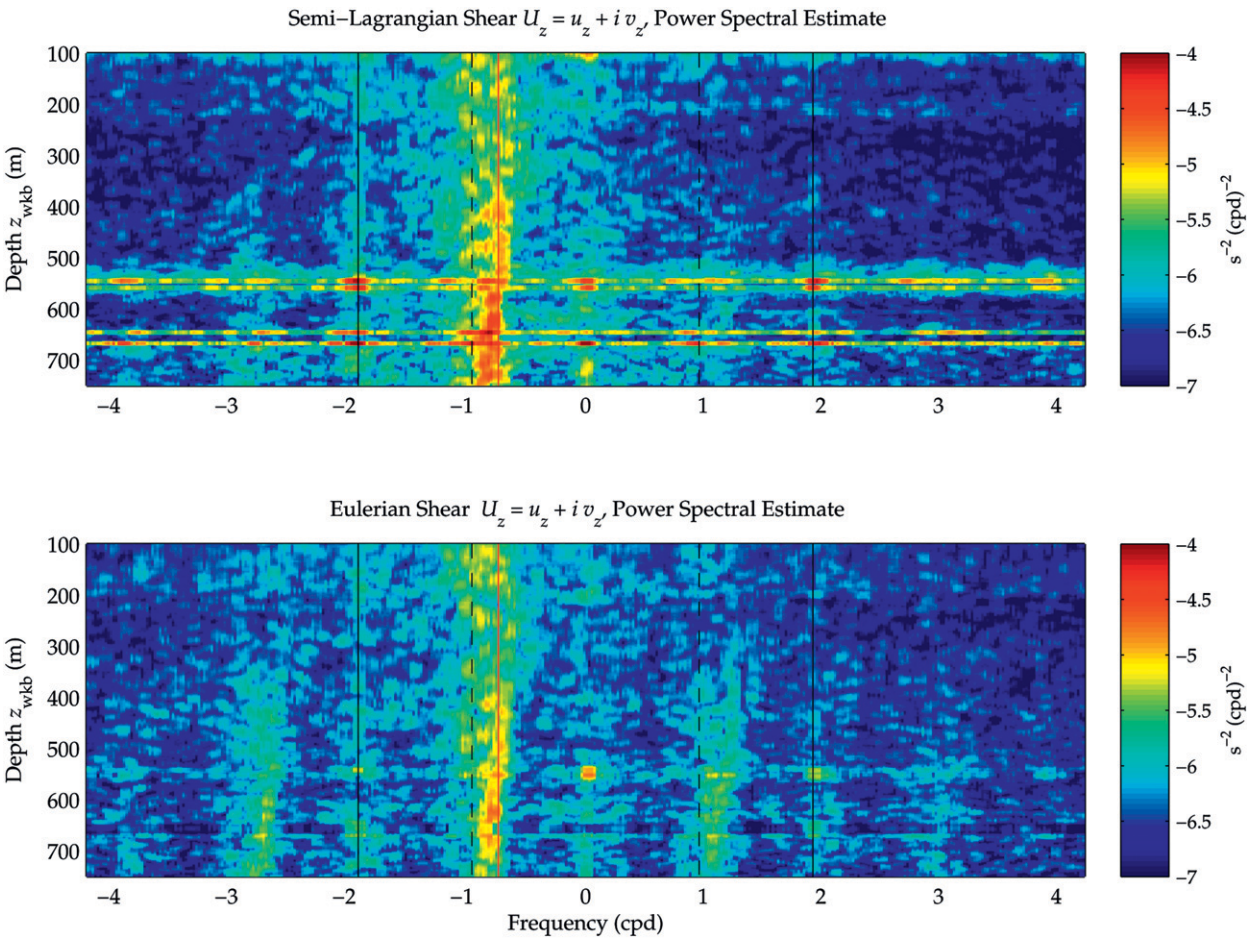

FIG. 10. Two-sided power spectral estimates of vertical shear $\mathcal{U}_z = (u_z + iv_z)$ in (top) semi-Lagrangian and (bottom) Eulerian coordinates. As in Fig. 9, but for shears, which emphasize small-vertical-scale, low-frequency waves likely to be involved in PSI interactions with the low-mode tide. Here, variance is concentrated in the inertial–diurnal f–D_1 band. Very little shear is visible at tidal frequencies. As in the velocities, the Eulerian shear spectra show images of the f–D_1 band, which have been shifted to the left and right by multiples of M_2.

Cross-bispectral methods were previously used by Sun and Pinkel (2012) to analyze low-frequency–high-frequency energy transfers, but PSI is driven by a different set of nonlinear terms than the interaction they considered. As a result, the bispectra we develop here will take a form distinct from theirs.

While our bispectral analysis will be carried out using frequency domain signals, we can incorporate some vertical wavenumber information to maximize the signals from PSI triads, which theory predicts will be widely scale-separated, while minimizing noise from motions which cannot participate in resonant interactions. Thus we form a cross-bispectrum $B_{X,Y,Z}$, between quantities (X, Y, Z), which are weighted toward triads with the preferred vertical scales for PSI, instead of estimating $B_u(\omega_1, \omega_2, \omega_1 + \omega_2)$ directly. We represent motions at the subharmonic frequencies (ω_1, ω_2) using the vertical shears of horizontal velocity (Fig. 5) in complex form $\mathcal{U}_z$. For the long-scale motions at the primary frequency $\omega = \omega_1 + \omega_2$, we use isopycnal displacements η. From (45), we also anticipate that nearly all of the motions associated with waves at subharmonic frequencies are represented in the positive-frequency (anticyclonic) Fourier coefficients $\hat{\mathcal{U}}(\omega_1), \hat{\mathcal{U}}(\omega_2), \omega_1, \omega_2 > 0$. Thus we estimate a cross-bispectrum of the form

$$B_{-\mathcal{U}_z,\mathcal{U}_z,\eta}(\omega_1, \omega_2, \omega_1 + \omega_2) = E[-\hat{\mathcal{U}}_z(\omega_1)\hat{\mathcal{U}}_z(\omega_2)\hat{\eta}^*(\omega_1 + \omega_2)], \quad \omega_1, \omega_2 > 0, \tag{50}$$

where we have used the fact that η is real, so that $\hat{\eta}_* = \hat{\eta}^*$. From $B_{-\mathcal{U}_z,\mathcal{U}_z,\eta}$, we can use the polarization relationships (27) to recover B_u.

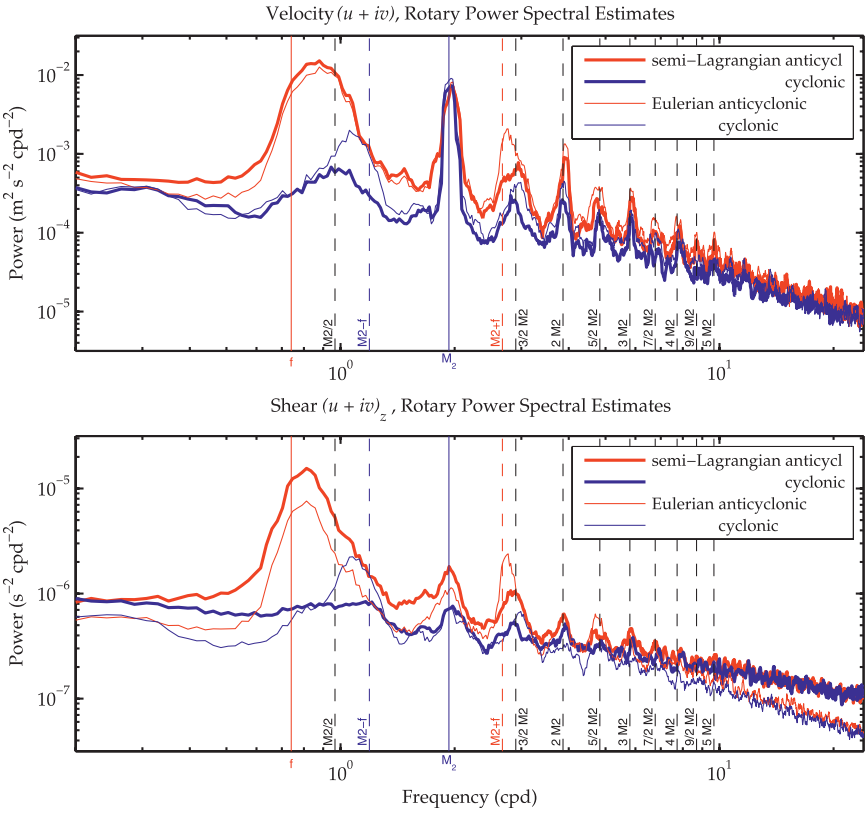

FIG. 11. Depth-averaged power spectral estimates of complex velocity and shear $\mathcal{U} = (u + iv)$. Heavy lines indicate semi-Lagrangian estimates, while thin lines are Eulerian. Anticyclonic ($\omega < 0$) and cyclonic ($\omega > 0$) frequencies are indicated in red and blue, respectively. (top) Depth-averaged velocity spectra with the effects of tidal Doppler shifting clearly seen. The tidal peak shows nearly equal variance in both coordinate frames, while the semi-Lagrangian frame retains more variance in the near-inertial peak. Away from the inertial cusp, Eulerian spectra show higher variance due to Doppler shifted from frequencies near f. Spectral contamination at $(\pm M_2 \pm f)$ is strong enough to obscure the $-M_2/2$ peak in the Eulerian frame. (bottom) Shear spectra with the subharmonic peak contained in small-scale waves, which are emphasized by taking semi-Lagrangian shears, but are again covered by $(\pm M_2 \pm f)$ contamination in the Eulerian frame. The pattern of Eulerian spectral contamination is generally similar to that seen in the velocities, but with more severe effects because of the weighting toward high wavenumbers introduced by taking shears.

Either form of the bispectrum determines the PSI energy transfer rate, up to coefficients which are functions of the triad frequencies and wavenumbers. Comparing (33) to (50),

$$\mathcal{G} = \hat{u}_1 \hat{u}_2 \hat{U}^*(ik) \tag{51}$$

$$= \frac{i}{m_1}\hat{\mathcal{U}}_{1z}\left(\frac{\omega_1}{\omega_1 + f}\right)\frac{i}{m_2}\hat{\mathcal{U}}_{2z}\left(\frac{\omega_2}{\omega_2 + f}\right)m\omega\hat{\eta}^* \tag{52}$$

$$= -\hat{\mathcal{U}}_{1z}\hat{\mathcal{U}}_{2z}\hat{\eta}^*\left(\frac{\omega_1}{\omega_1 + f}\right)\left(\frac{\omega_2}{\omega_2 + f}\right)\left(\frac{m\omega}{m_1 m_2}\right) \tag{53}$$

$$= B_{-\mathcal{U}_z \mathcal{U}_z, \eta}\left(\frac{\omega_1}{\omega_1 + f}\right)\left(\frac{\omega_2}{\omega_2 + f}\right)\left(\frac{m\omega}{m_1 m_2}\right). \tag{54}$$

The PSI resonance condition requires $m_1 \approx -m_2$. From the predominantly upward energy propagation of the tide in HOME Nearfield, we infer that $m < 0$. Therefore, $(m\omega/m_1 m_2) > 0$, and a positive real part of $B_{\mathcal{U}_z \mathcal{U}_z, \eta}$ is associated with positive energy transfers. (The reverse would be true for a downward-propagating tide.)

Sample realizations of (50) are formed by segmenting the time series of the inputs $\mathcal{U}_z$ and η, at each reference depth, into a series of 50%-overlapping subrecords, each of length 1488 samples or approximately 4 days, equivalent to eight M_2 tidal periods or approximately three local inertial periods. A single bispectral realization is computed from each subrecord, which is tapered using a 5% cosine window before Fourier transforming. All realizations from a set of depths are averaged together

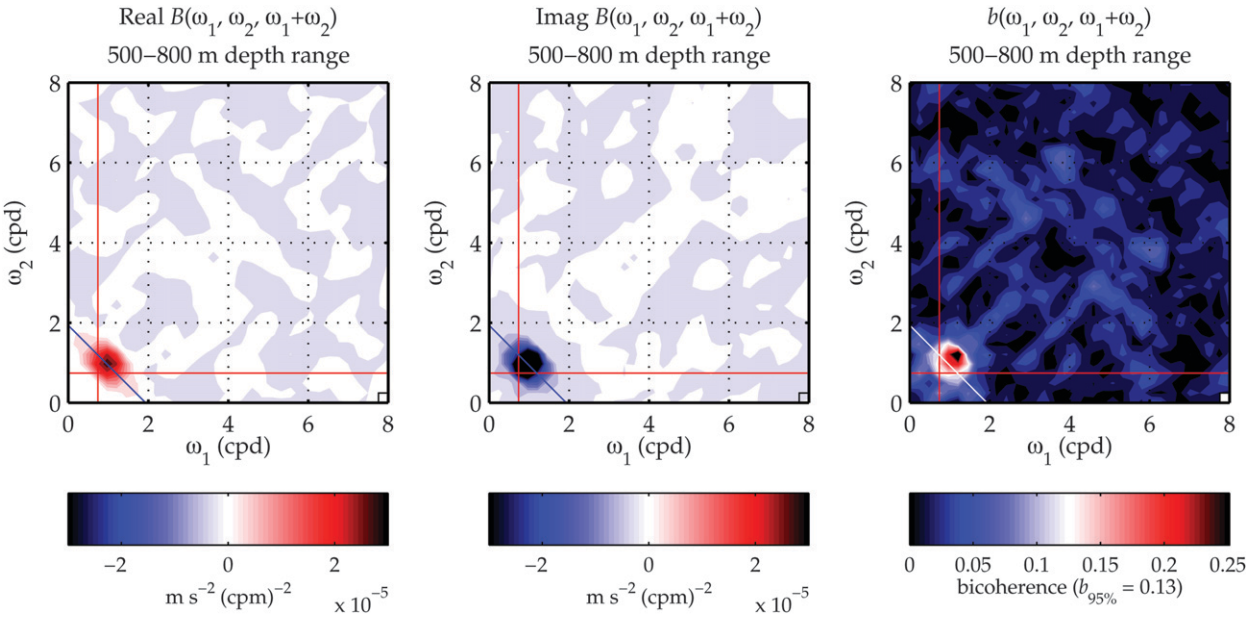

FIG. 12. Bispectral estimates for the 500–800-m-depth range. Bispectra are plotted on coordinates (ω_1, ω_2). Red lines indicate the local inertial frequency f, while the blue line indicates frequencies which sum to the semidiurnal frequency M_2. The size of a (bi)frequency bin is indicated by the small square in the bottom right-hand corner of each plot. (left) The real part of the bispectrum $B_{-\mathcal{U}_z\mathcal{U}_z,\eta}(\omega_1, \omega_2, \omega_1 + \omega_2)$ associated with energy transfers to subharmonic waves, (middle) imaginary part, and (right) bicoherence b. The color axis is centered on the 95% significance threshold $b_{95\%} = 0.13$.

to form the expected value in (50). Finally, a smoothing operation is applied in the bifrequency plane, using a simple version of the hexagonal window discussed in Birkelund and Hanssen (2009), which we form by the composition of two-point smoothing along each of the three input frequencies

$$W_3 = \begin{bmatrix} 1 \\ 1 \end{bmatrix} \times [1 \quad 1] \times \begin{bmatrix} 1 & 0 \\ 0 & 1 \end{bmatrix} = \begin{bmatrix} 1 & 1 & 0 \\ 1 & 2 & 1 \\ 0 & 1 & 1 \end{bmatrix}, \qquad (55)$$

and then normalizing to make the total weight unity.

Since the shear spectra (Fig. 5) show a progression with depth of the peak frequency from near-inertial to near-diurnal, we estimate the bispectrum over two depth ranges: an upper range of 300–600 m and a slightly overlapping lower range 500–800 m (WKB depths).

In estimating significance thresholds for b, we regard measurements separated by 50 m in the vertical, or approximately a half-wavelength of the characteristic wavelength seen in the shear plots (Fig. 5), as independent. Combining six independent measurements over each 300-m depth range with eight independent transform lengths in time yields 96 degrees of freedom (dof), which is improved by a factor of 4 by smoothing using (55), giving an estimated 95% bicoherence threshold of $b_{95\%} \approx \sqrt{6/384} \approx 0.125$.

b. 500–800-m-depth range

Bispectra for the lower depth range, which spans 500–800 m in depth (368–776 m in unstretched coordinates) are presented in Fig. 12. The real part of the bispectrum (left panel), which is associated with energy transfers, has a positive peak centered at $(\omega_1, \omega_2, \omega_1 + \omega_2) = (M_2/2, M_2/2, M_2)$, indicating positive transfer to subharmonics of the semidiurnal frequency. A peak with about twice the height is present at the same location in the imaginary part of the bispectrum (middle panel), which is not associated with energy transfers. The bispectra are symmetric, since both ω_1 and ω_2, are represented by identical inputs $\mathcal{U}_z$. No other bispectral variance is apparent in the region shown, $0 < \omega_1, \omega_2 < 8$ cpd.

The bicoherence b is shown in Fig. 12 (right panel). The color scale is centered on $b_{95\%}$, so that values of white or above represent significant bicoherences ($b > b_{95\%} \approx 0.13$). The peak in b is skewed slightly up-frequency relative to the bispectral peak, possibly as a result of normalization by the large spectral densities near the inertial frequency.

PREFILTERING BY VERTICAL PROPAGATION

The choice of cross-bispectral inputs in (50) weights the bispectra toward triads, which have vertical scales consistent with PSI. We can further improve our use of the spatial information contained in the profiles. Since

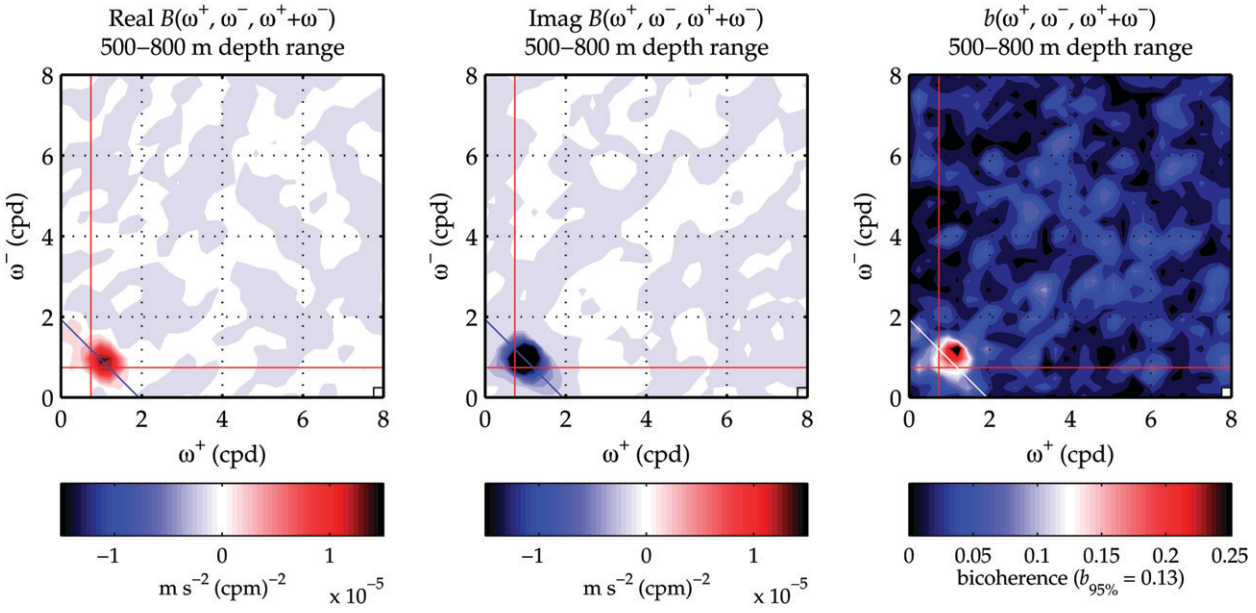

FIG. 13. Up–down-prefiltered bispectra for the 500–800-m-depth range. As in Fig. 12, but the shears representing (ω_1, ω_2) have been prefiltered using a 2D Fourier transform into components associated with upward and downward energy propagation, respectively. Frequencies are denoted by (ω^+, ω^-) to indicate the component that varies along each frequency axis. (left) The real part of the bispectrum $B_{-\mathcal{U}_z\mathcal{U}_z,\eta}(\omega^+, \omega^-, \omega^+ + \omega^-)$ is associated with energy transfers to subharmonic waves, (middle) imaginary part, and (right) bicoherence b.

the PSI resonance condition requires the subharmonic waves to propagate in opposite vertical directions, we "prefilter" the shears $\mathcal{U}_z$ into components $\mathcal{U}_z^+, \mathcal{U}_z^-$ associated with upward and downward energy propagation, respectively, by 2D (ω, m)-Fourier transforming the shear data, retaining only the quadrants associated with negative (or positive) vertical propagation, and then inverse transforming. Prefiltered bispectral estimates are formed using the resulting frequency Fourier coefficients

$$B_{-\mathcal{U}_z^+\mathcal{U}_z^-,\eta}(\omega^+, \omega^-, \omega^+ + \omega^-) = E[-\widehat{\mathcal{U}_z^+}(\omega^+)\widehat{\mathcal{U}_z^-}(\omega^-)\hat{\eta}^*(\omega^+ + \omega^-)], \quad \omega^+, \omega^- > 0. \tag{56}$$

Prefiltered bispectra from the 500–800-m-depth range are shown in Fig. 13. The real part of the bispectrum is now slightly asymmetric because ω^+ and ω^- are represented by different quantities. However, the significance of the bicoherent peak near $(M_2/2, M_2/2, M_2)$ remains essentially unchanged by prefiltering.

While prefiltering selects for subharmonic waves which can form resonant triads due to their wave vector orientations, we can also filter the bispectral inputs to suppress resonant triads. We do this by forming bispectra using same-signed shears (both upward or both downward), for which wavenumber resonance is theoretically impossible. The resulting "defiltered" bispectra, which serve as a test for PSI resonance, are shown in Fig. 14, next to the prefiltered version. Only the prefiltered bispectra show a significant energy transfer, while the defiltered bispectra, whose inputs are dissonant in wavenumber, find essentially zero bicoherence. The results are consistent with the resonant theory, which requires a PSI triad to simultaneously satisfy both frequency and wavenumber resonance.

c. 300–600-m-depth range

In the upper depth range, 300–600 m (218–470 m unstretched), the PSI-associated bispectral peak (not shown) is weaker than in the lower depth range, with variances in the upper range that are half to a third as large. Bicoherences fail to be significant at the 95% level. To see whether statistical significance can be attained if the ambient noise from nonresonant wave energy is reduced, we apply the same prefiltering used in the lower depth range to the 300–600-m data. Up/down-prefiltered bispectra from the shallower depth range, shown in Fig. 15, have a positive peak located near $(M_2 - f, f, M_2)$. A smaller negative peak is also present near $(M_2 - (1/3)f, (2/3)f, M_2)$, which would make one of the participants subinertial. Both peaks, however, still fall below 95% significance.

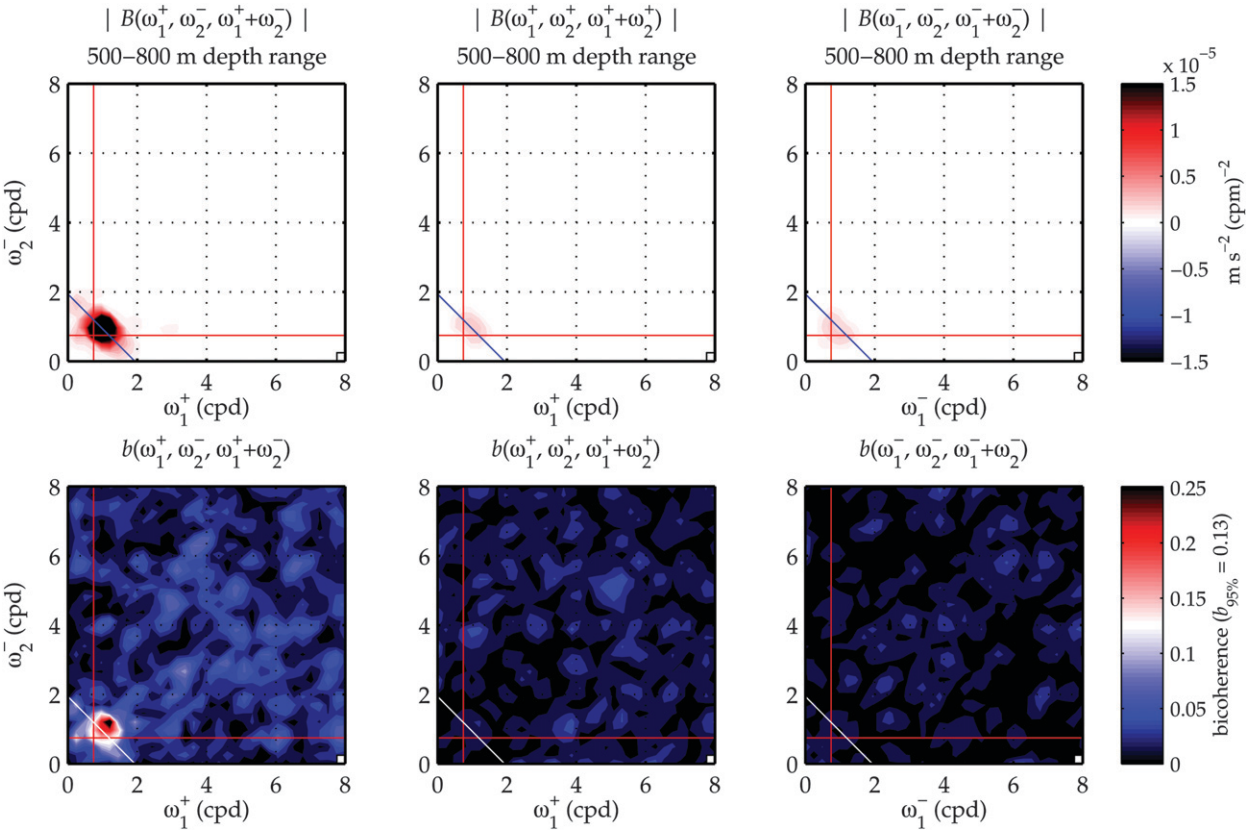

FIG. 14. Prefiltered vs defiltered bispectra, 500–800-m-depth range. (left) Up–down (ω^+, ω^-) prefiltered bispectrum and bicoherence, as in Fig. 13, but here showing the absolute value of the bispectrum. Significant bicoherences associated with PSI frequency and wavenumber resonance are found. (middle) Up–up defiltered bispectrum and bicoherence, formed after filtering to pass two upward-propagating shear fields. (right) Down–down defiltered bispectrum and bicoherence, using two downward-propagating shear fields. Both defiltered results show some bispectral variance near the frequencies involved in PSI frequencies, but as predicted by the wavenumber resonance condition (1), the signals are not bicoherent.

The detail view presented in Fig. 16 summarizes the bispectral results from both depth ranges. The real bispectra are plotted only where the bicoherence exceeds a fixed threshold. In the lower depth range (left), the bispectral peak at $(\omega^+, \omega^-, \omega^+ + \omega^-) = (M_2/2, M_2/2, M_2)$ still remains. There is some suggestion of a shift in the triad's location, with the upward-propagating subharmonic tending slightly above $M_2/2$, with the downward subharmonic slightly below. This may simply reflect the fact that the f–D_1 shears at shallower depths have more variance near f rather than D_1 (Fig. 10).

In the upper depth range (right), the bispectrum is presented using a reduced significance threshold of 90% to show the location of the largest energy transfers. Here, the downward-propagating waves that seem to participate in PSI tend to have even lower frequency, so that the peak positive energy transfer is centered on $(M_2 - f, f, M_2)$. However, the peak never reaches the 95% significance threshold, so that the perceived frequency shift is likely a statistical artifact, rather than evidence of PSI with near-inertial motions.

5. Depth–time maps of PSI energy transfer

Triad interactions are traditionally represented somewhat abstractly as Feynman diagrams in wavenumber space, for example, Hasselmann (1966). Bispectral results give a statistical view of the interaction. Can one watch such an interaction unfold in the depth–time domain? Here we attempt to visualize the PSI interaction in the Nearfield. The frequencies and scales that are associated with bicoherent energy transfers are first isolated by filtering $\mathcal{U}_z$ to keep only anticyclonic shears and then frequency bandpassing both $\mathcal{U}_z$ and η. The subharmonic passband for $\mathcal{U}_z$ includes one-half octave on either side of the subharmonic frequency $M_2/2$, or 1/16–1/34 cph. The semidiurnal band for η is 1/8–1/15 cph. All filters are 6th-order, Butterworth-derived, phase-preserving

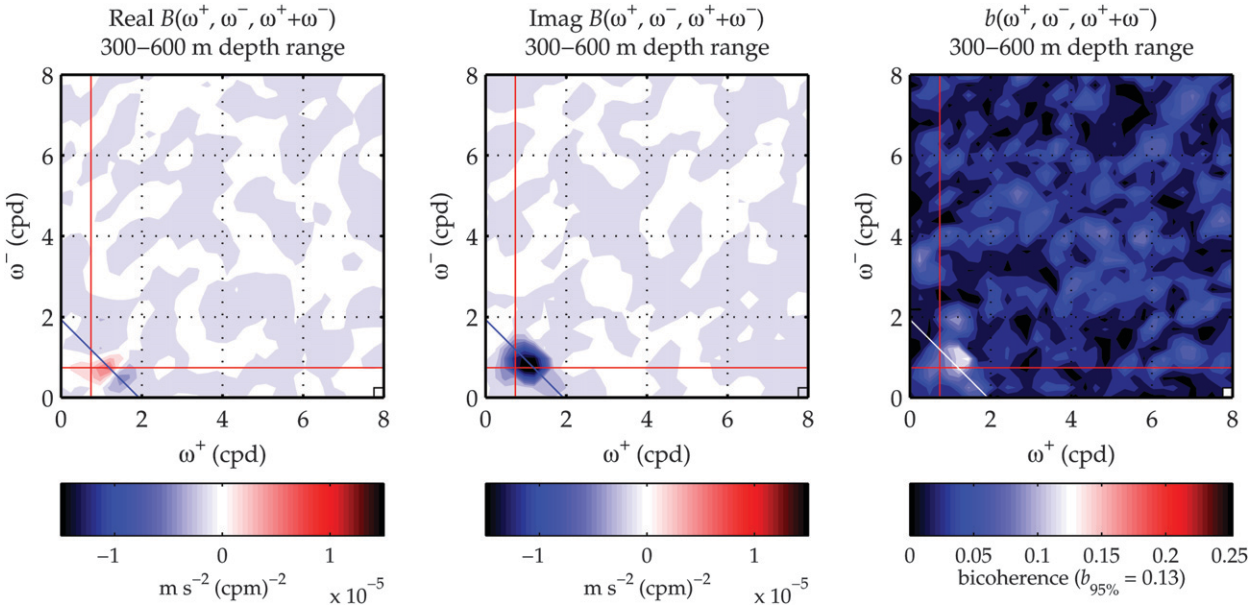

FIG. 15. As in Fig. 13, but for the 300–600-m-depth range. The (f, $M_2 - f$, M_2) peak achieves significance at the 90% level, but not 95%.

filters. From the band-limited inputs, the PSI source term (32) is estimated at all points in depth and time

$$\mathcal{G}' \approx u_1 u_2 U_x \left(1 + \frac{f^2}{\omega_1 \omega}\right)\left[1 \mp \left(\frac{\omega_2^2 - f^2}{\omega^2 - f^2}\right)^{1/2}\right] + \text{c.c.}$$
$$\approx \mathcal{U}_z \mathcal{U}_z \eta \left(\frac{-m\omega}{m_1 m_2}\right), \qquad (57)$$

where a nominal tidal vertical wavenumber of $m = \pi/4000$ m $\times$ $N(z)/N_0$ and subharmonic wavenumbers $m_1 = m_2 = 2\pi/120$ m $\times$ $N(z)/N_0$ are used.

Figure 17 shows the inputs to (57): the bandpassed, WKB-scaled and stretched M_2 displacements and prefiltered f–D_1 shears. The intermediate product formed between the shears, included in the bottom panel, shows a pattern of nearly vertical crests and much longer

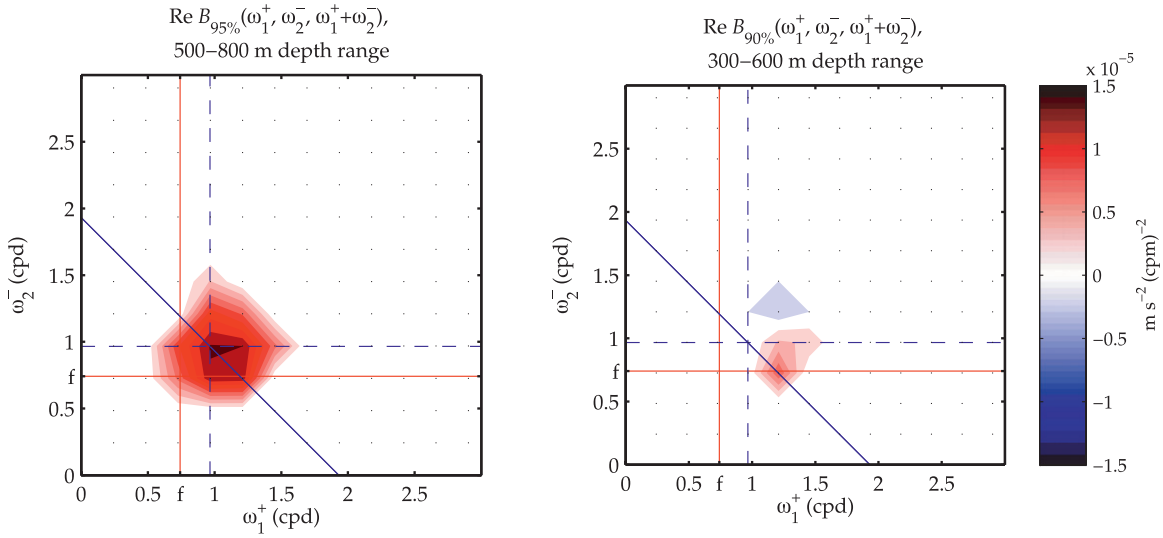

FIG. 16. Detail view showing bicoherent energy transfers. As in left panels of Figs. 13 and 15, but the detail view here has been masked to show only values of the real bispectrum where the bicoherence exceeds a fixed threshold. (left) $B(\omega_1, \omega_2)$ in the 500–800-m-depth range, $b(\omega_1, \omega_2) > b_{95\%}$, showing PSI energy transfers between waves at the semidiurnal frequency and subharmonic triad members. (right) $B(\omega_1, \omega_2)$ in the 300–600-m-depth range, with a *reduced* significance threshold $b > b_{90\%}$ to show details of the bispectral peak located at (f, $M_2 - f$, M_2).

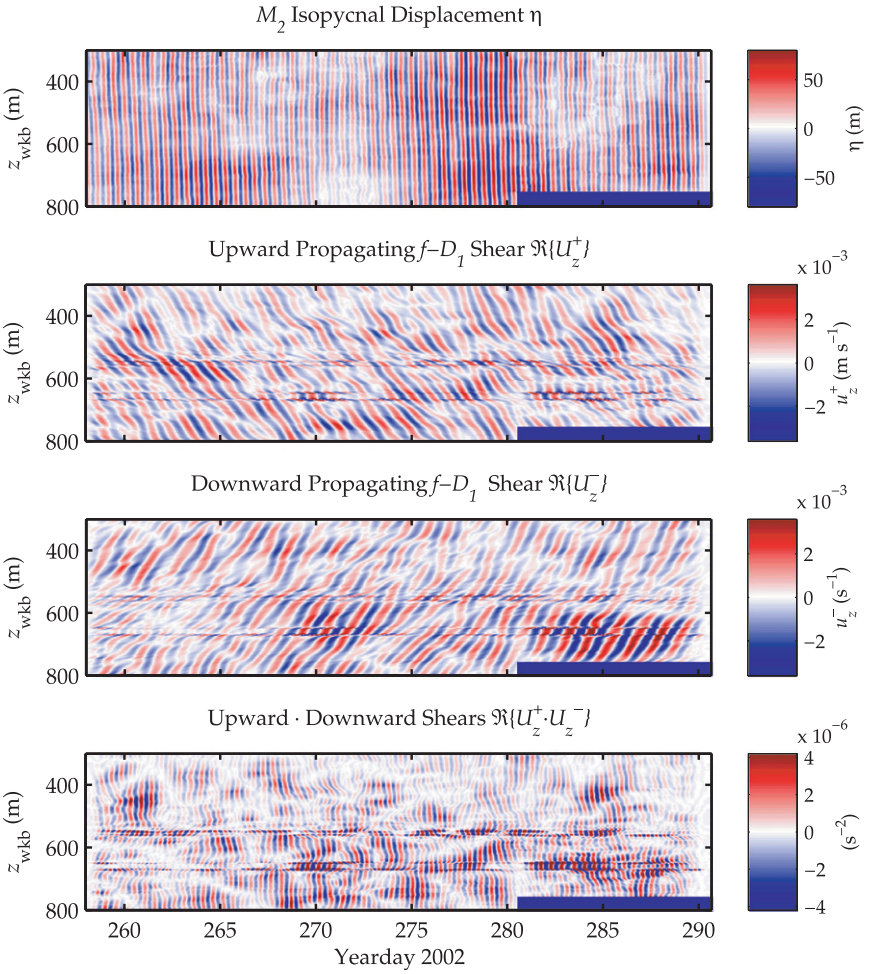

FIG. 17. Filtered and bandpassed psi participants. (top) M_2 displacement. (top middle) Upward-propagating prefiltered f–D_1 shear $\mathcal{U}_z^+$. (bottom middle) Downward-propagating prefiltered f–D_1 shear $\mathcal{U}_z^-$. (bottom) Product of upward and downward shears $\mathcal{U}_z^+\mathcal{U}_z^-$. Crests of the upward–downward product are nearly vertically aligned, allowing pairs of high-mode shears to interact resonantly with much lower-mode M_2 waves.

vertical scales relative to the individual shears. It is this shift in scales that allows the product of the two shears to be resonant with the low-mode semidiurnal tide.

Estimates of the energy transfer product (57) using WKB-scaled quantities are presented in Fig. 18. Maps are formed using both the full shear record and the prefiltered shears. The prefiltered products are doubled to account for energy gain by both upward- and downward-propagating waves. Depth profiles, plotted at the right of each depth–time map, show that the two estimates find similar time-averaged energy transfer rates. The prefiltered estimate provides a clearer picture of regions where continuing interactions over several wave periods result in net energy transfer, as indicated in the map by patches of consistent red or blue color. The overall picture is predominantly red below about 500-m (scaled) depth, as expected from the bispectral estimates of the previous section, which find a positive net energy transfer to the subharmonic waves. There are, however, clearly visible blue areas, in particular above 500-m (scaled) depth on days 277–282 and at 600–700-m (scaled) depth on days 283–287. The latter blue patch occurs between spring tides (as seen in the displacements, Fig. 17, top) and appears to be associated with a downward-propagating f–D_1 wave group (Fig. 17, third panel), which exchanges energy with the semidiurnal tide rather than simply receiving energy.

Energy transfers are also estimated for defiltered (up–up and down–down) shears (Fig. 19). Large-variance areas here are crossed by alternating, slanted stripes, indicating energy transfers that are not resonant but instead oscillate in depth and time. As a result, the time-averaged

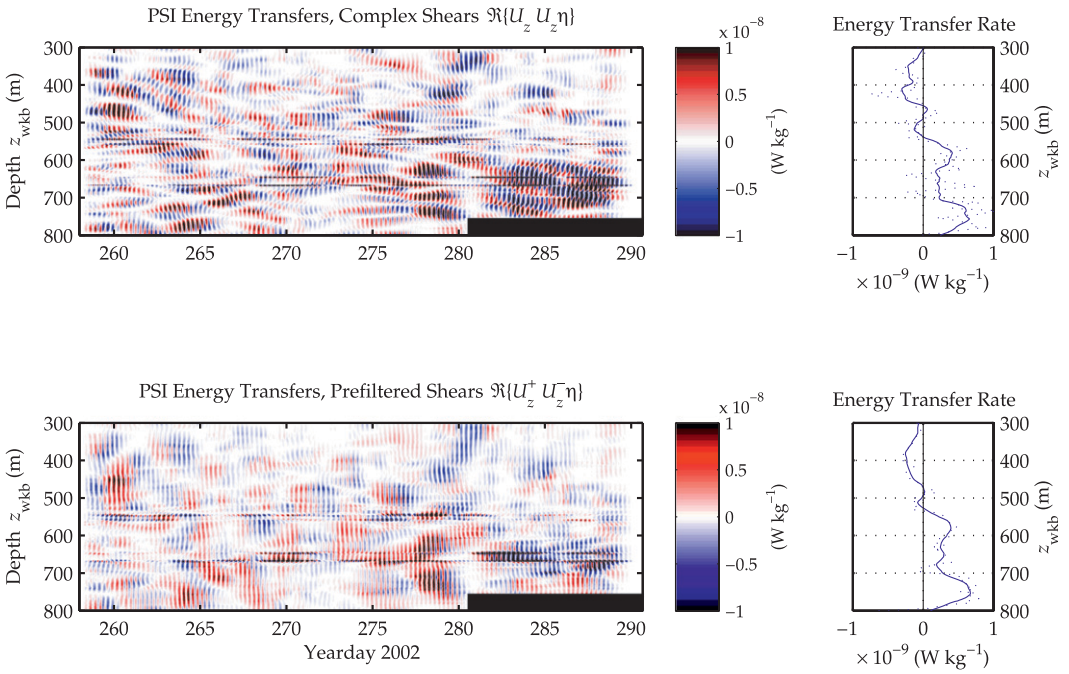

FIG. 18. PSI energy transfers estimated using unfiltered and prefiltered shear fields. Time-averaged energy transfer profiles, which are smoothed using a 100-m (scaled) moving average, are plotted to the right of each record. (top) Using the full f–D_1 shear field $\mathcal{U}_z$, containing both upward and downward propagating wave energy. (bottom) Using prefiltered shears $\mathcal{U}_z^+\mathcal{U}_z^-$ from Fig. 17. The time-averaged energy transfer rates are nearly identical between the plots, but the use of prefiltered shears allows the interactions to be more clearly seen.

energy transfers, plotted to the right, are nearly zero when averaged over a few wavelengths. The oscillatory character of the interaction product in the nonresonant patches emphasizes the need for sufficient temporal and spatial coverage when estimating bispectra.

The estimate (57), of PSI energy transfers to the shortest-scale subharmonic waves, depends on all three interacting vertical wavelengths m, m_1, and m_2. Using velocities $\mathcal{U}$ instead of shears $\mathcal{U}_z$, an alternative estimate can be formed which does not depend on knowing the subharmonic wavelengths m_1 and m_2,

$$\mathcal{G}'_{\text{velocity}} \approx \mathcal{U} \times \mathcal{U} \times \eta(m\omega). \tag{58}$$

By removing the weighting toward short-scale f–D_1 waves, a wider range of wavelengths in η are included in the resonant transfer estimate. In Fig. 20, we present both the estimate formed from shears (top) and the estimate from velocities (bottom). To give estimates in meaningful physical units, both versions are here computed using unscaled quantities, and the results are shown using true, rather than WKB-scaled, depths. While similar structures appear in both plots, the energy transfer estimates derived from velocities below 400-m true depth are about 3 times larger, at about 2×10^{-9} W kg^{-1}, than the transfers estimated from shears, which are about 7×10^{-10} W kg^{-1}. An oscillatory structure that coincides with a downward-propagating f–D_1 wave shortly after day 280 is apparent in the velocity-derived estimate, but it does not seem to be associated with a large net energy transfer of either sign. The large discrepancy between the shear- and velocity-derived energy transfer estimates can be explained by considering the implicit band-filtering imposed by taking vertical shears. If, for example, only $\frac{2}{3}$ of the effective bandwidth of interacting subharmonic waves is captured by the shears, then the semidiurnal waves able to interact with the subharmonic waves will be similarly band limited. Since the energy transfer term (32) is a triple product, only $(\frac{2}{3})^3$ of the energy transfers will be captured in such a band-limited estimate.

A nominal semidiurnal vertical wavenumber of $m \approx \pi/4000$ m, which appears in both (57) and (58), is chosen to reflect the vertical wavelength of a mode one tide. Since the interaction likely involves several modes of the M_2 tide, the true transfer rates can easily be larger by factors of 2 or more through an increase in effective m. The fractional contribution from different tidal modes is beyond the scope of this study, but we emphasize that the unknown tidal vertical wavenumber m is a large source of uncertainty in our energy transfer estimates.

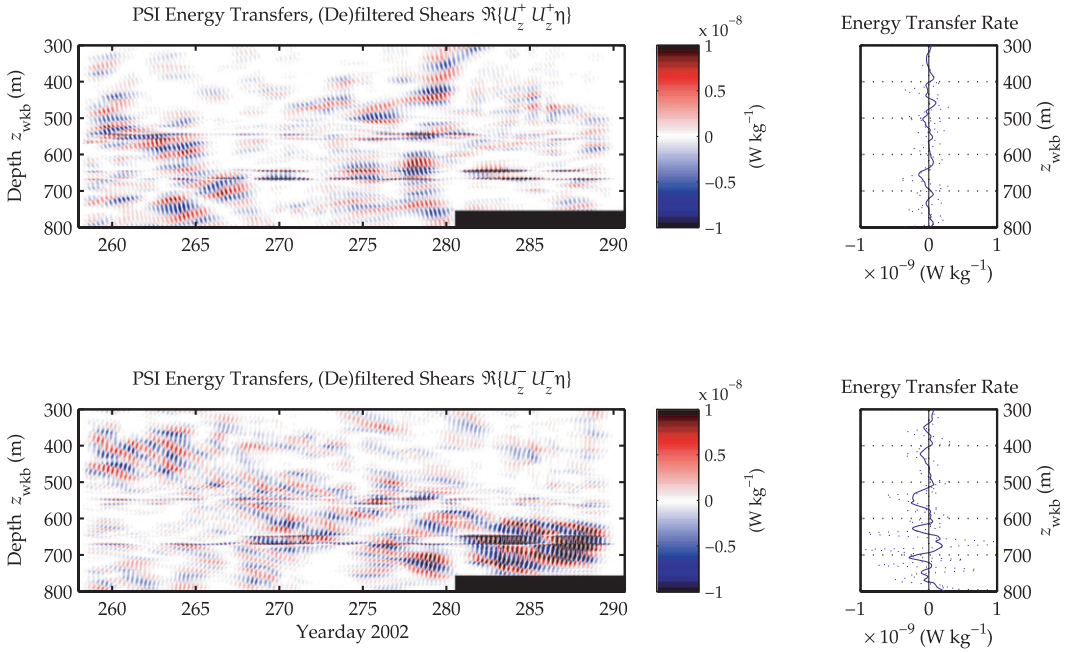

FIG. 19. PSI energy transfers estimated using defiltered shear fields. As in Fig. 18, but using pairs of shear fields that cannot form resonant triads with the low-mode tide. (top) Using up–up shears $\mathcal{U}_z^+$, $\mathcal{U}_z^+$. (bottom) Using down–down shears $\mathcal{U}_z^-$, $\mathcal{U}_z^-$. In both plots, the alternating blue and red stripes indicate oscillating energy transfers rather than resonance.

6. Discussion

In light of the energy transfer estimates obtained here, is PSI likely to be relevant to tidal decay and mixing? The magnitude of turbulence dissipation estimates suggests that PSI and other weakly nonlinear energy transfers are dominated by strongly nonlinear processes, such as direct breaking of the internal tide (Klymak et al. 2008), in the immediate vicinity of Kaena Ridge. However, it is possible to estimate the relative contribution of PSI to local tidal mixing in the Nearfield, against a background of strongly turbulent processes. If we model PSI decay simply as an attenuation process, so that the tidal energy flux is a function of distance r divided by a characteristic decay length scale λ_{PSI}

$$E(r) = E_0 \exp(-r/\lambda_{\mathrm{PSI}}),$$

then λ_{PSI} can be estimated from the observed PSI energy transfers. Integrating our estimated PSI transfer rates from 200 m to the bottom of our profiles yields an areal density of 8×10^{-4} W m^{-2}. Using an estimated semidiurnal energy flux of about 1100 W m^{-2} at the HOME Nearfield site (Rainville and Pinkel 2006a), the implied decay scale is

$$\lambda_{\mathrm{PSI}} \approx (0.84\,\mathrm{mW\,m^{-1}}/1100\,\mathrm{W\,m^{-2}})^{-1} \approx 1400\,\mathrm{km}.$$

Assuming that PSI acts steadily along the path of the M_2 tidal beam, about 4.5% of the semidiurnal energy flux will be transferred from the tide to subharmonic waves within 60 km from the ridge. If the subharmonic waves are dissipated locally, then PSI could account for a small but significant fraction of the estimated 8%–25% energy loss from the internal tide to turbulence within 60 km Klymak et al. (2006).

A decay length scale of 1400 km is reasonably consistent with studies of long range M_2 tidal propagation from Hawaii, which find that the low-mode M_2 tidal fluxes decay only modestly (and the mode-one tide hardly at all) within 1000 km of the ridge (Rainville and Pinkel 2006b; Rainville et al. 2010; Zhao et al. 2010), and that the tide retains significant energy even after propagating more 3500 km across the Pacific basin (Zhao and Alford 2009). It is difficult to further constrain the PSI decay rate using flux estimates from either moorings or altimetry. Horizontal variability in M_2 tidal fluxes far exceeds the predicted variations owing to PSI decay. For the southward-propagating beam, Rainville and Pinkel (2006b) argue that mesoscale eddies are already sufficient to explain any decay inferred from the altimetric record. Meanwhile, the attenuation of the northward beam emanating from Hawaii is obscured by both refraction and interference from multiple sources, and as a result flux estimates do

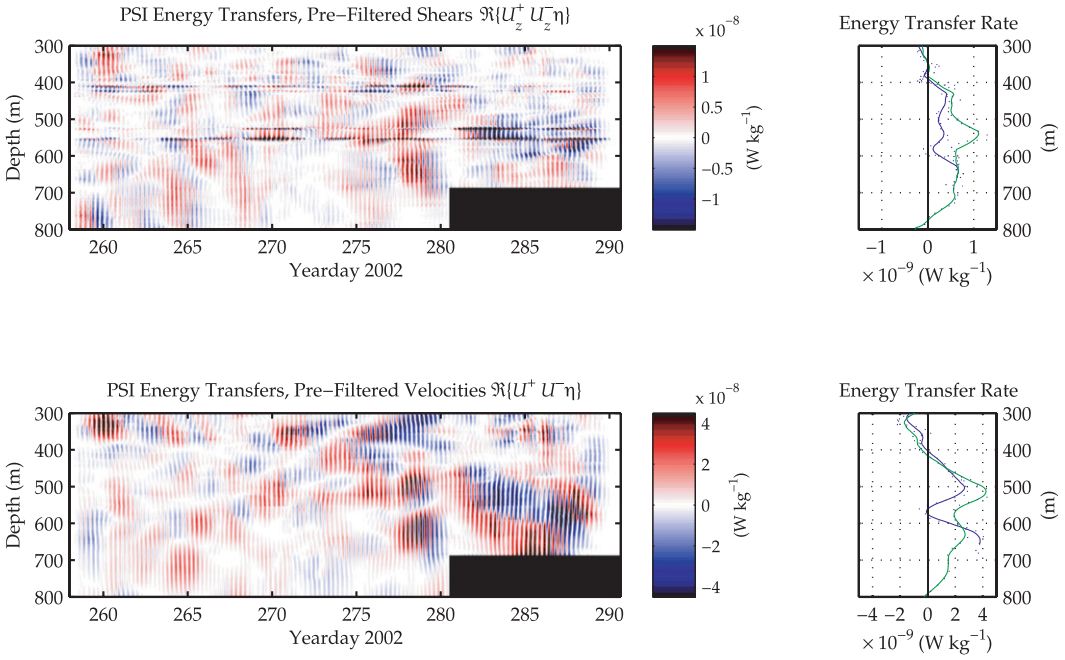

FIG. 20. PSI energy transfers estimated using prefiltered shears and velocities. As in Fig. 18, but here unscaled shears and velocities are used, and the results are plotted using a depth coordinate of meters. Time-averaged energy transfer profiles, which are smoothed using a 100-m moving average, are plotted to the right of each record. The blue lines indicate averages over the entire time range, while the green averages end on day 281 but include the entire depth range. Note the *different* color scales used for the upper and lower plots. (top) Energy transfer estimates using prefiltered shears $\mathcal{U}_z^+, \mathcal{U}_z^-$, as in Fig. 18, which are weighted toward subharmonic waves with short vertical scales. The average energy transfer rate for 400–800 m is about 7×10^{-10} W kg^{-1}. (bottom) Energy transfer estimates using prefiltered velocities $\mathcal{U}^+, \mathcal{U}^-$, include subharmonic waves with a wider range of vertical scales. The averaged energy transfer rate over 400–800 m is about 2×10^{-9} W kg^{-1}, or 3 times larger than the average estimated using the shears.

not decay monotonically with distance along the IWAP mooring line (Alford et al. 2007; Zhao et al. 2010).

Our midlatitude PSI energy transfer rate is 4–5 times less dense by area than PSI transfers near the critical latitude, for which Alford et al. (2007) inferred a rate of 2.5×10^{-3} W m^{-2}. Nevertheless, the predicted loss to the M_2 tide along its ≈800-km propagation from the north edge of Kaena Ridge toward the critical latitude is about 40%. Even if we were to take half that value as a conservative estimate, the net loss would still be comparable to the 10%–20% attributed to near-inertial PSI within 50 km of the critical latitude (Alford et al. 2007). It seems possible, in light of the distances traveled, that the integrated PSI decay en route to the critical latitude is as significant for the M_2 tide as its PSI decay upon reaching 28.8°. However, it should be emphasized that PSI is a nonlinear process, which depends on the relative phases and amplitudes of each of the participants represented in the source term (32). Any variability in the M_2 fluxes or the subharmonic–near-inertial field is likely to disrupt the phase locking that is essential to subharmonic growth. Neither of these factors is considered in our simple attenuation model. Therefore, we suggest that the PSI decay rates we estimate here be taken as upper-bound estimates.

7. Summary

Near Kaena Ridge, Hawaii, the generation of the semidiurnal internal tide sets the stage for PSI. Significant wave energy is observed in high-mode, near-diurnal waves, which appear to be distinct from near-inertial, wind-generated waves. The main results of this study follow from bispectral analysis. Bispectra are computed using proxies for the triad members, which emphasize the vertical scales likely to be involved in a PSI-like interaction. Shears are used to emphasize the potential high-wavenumber recipients of PSI energy transfers, while vertical velocities represent the low-mode waves at the source (sum) frequency. The resulting cross-bispectra find statistically significant energy transfers between pairs of near-diurnal waves and the M_2 tide in the 500–800-m (scaled) depth range. While large bispectral values are also found in the upper, 300–600-m (scaled) depth range, they are not associated with

significant bicoherences and must be regarded as statistical artifacts.

To test the PSI wavenumber resonance condition, we also compute bispectra using shears, which have been prefiltered into upward- and downward-propagating components. The results are consistent with the prediction of resonant theory. Significant bicoherences are found only when using shear pairs which have opposite-sign vertical propagation.

In our analysis, we have attempted to minimize contamination by mutual Doppler shifting, which has been previously thought to bias bicoherence estimates. Semi-Lagrangian coordinates have been used throughout, reducing spectral cross contamination by tidal heaving of isopycnals. While the Eulerian velocity and shear spectra show Doppler-shifted ''images'' of the near-inertial peak, which have been shifted by integral multiples of the M_2 frequency, these images are nearly absent in the semi-Lagrangian spectra. We suggest that the semi-Lagrangian bicoherences found here are associated with ''real'' nonlinear interactions, and not spectral contamination.

While the bispectral results offer statistical evidence of nonlinear interactions, the depth–time maps offer what is perhaps the most compelling evidence for PSI. The interaction products, which are formed from multiple shorter-scale, oscillatory records, show persistent patches with long vertical scales and uniform color, which are the signature of continuing energy transfers in depth and time. The presence of both red and blue regions in the map demonstrates that ''forward'' PSI energy transfers, from the semidiurnal tide to subharmonic waves, as well as ''reverse'' transfers are taking place in the Nearfield of HOME. The oscillatory character of ''non-resonance,'' shown most clearly in the defiltered depth–time map, manifests when candidate wave triads do not satisfy both frequency and wavenumber resonance. This simultaneous requirement underscores the need for sufficient temporal and spatial averaging when applying bispectral techniques.

Simple estimates of PSI decay along the path of M_2 propagation find that PSI may feed a small but significant fraction of the turbulent dissipation estimated for the internal tide within 60 km of the ridge. Longer-distance estimates are more uncertain, but suggest that the integrated PSI energy transfer along the tidal beam, equatorward of 28°N, may be comparable to or even exceed PSI observed near the critical latitude.

Acknowledgments. The authors thank Eric Slater, Mike Goldin, Lloyd Green, Mai Bui, Tyler Hughen, Tony Aja, and Luc Rainville for support in the design of instrumentation and collection of data at sea. Captain Tom Golfinos and the crew of the Research Platform *FLIP* provided exemplary support. Discussions with Bill Young, Jen MacKinnon, Jody Klymak, Jerry Smith, Mike Gregg, Tom Farrar, Kurt Polzin, and Wen-Yih Sun were extremely helpful.

This work was supported by the National Science Foundation and the Office of Naval Research.

REFERENCES

Alford, M., J. MacKinnon, Z. Zhao, R. Pinkel, J. Klymak, and T. Peacock, 2007: Internal waves across the Pacific. *Geophys. Res. Lett.,* **34,** L24601, doi:10.1029/2007GL031566.

Benney, D., and P. Saffman, 1966: Nonlinear interactions of random waves in a dispersive medium. *Proc. Roy. Soc. London,* **A289,** 301–320.

Birkelund, Y., and A. Hanssen, 2009: Improved bispectrum based tests for Gaussianity and linearity. *Signal Process.,* **89,** 2537–2546.

Bretherton, F., 1964: Resonant interactions between waves—The case of discrete oscillations. *J. Fluid Mech.,* **20,** 457–479.

Carter, G., and M. Gregg, 2006: Persistent near-diurnal internal waves observed above a site of M_2 barotropic-to-baroclinic conversion. *J. Phys. Oceanogr.,* **36,** 1136–1147.

Egbert, G. D., 1997: Tidal data inversion: Interpolation and inference. *Prog. Oceanogr.,* **40** (1–4), 53–80.

——, and R. Ray, 2001: Estimates of M2 tidal energy dissipation from TOPEX/Poseidon altimeter data. *J. Geophys. Res.,* **106** (C10), 22 475–22 502.

——, and S. Y. Erofeeva, 2002: Efficient inverse modeling of barotropic ocean tides. *J. Phys. Oceanogr.,* **19,** 183–204.

Elgar, S., and R. Guza, 1988: Statistics of bicoherence. *IEEE Trans. Acoust. Speech,* **36,** 1667–1668.

Frajka-Williams, E. E., E. L. Kunze, and J. A. MacKinnon, 2006: Bispectra of internal tides and parametric subharmonic instability. M.S. thesis, School of Oceanography, University of Washington, 26 pp.

Furuichi, N., T. Hibiya, and Y. Niwa, 2005: Bispectral analysis of energy transfer within the two-dimensional oceanic internal wave field. *J. Phys. Oceanogr.,* **35,** 2104–2109.

Gill, A. E., 1982: *Atmosphere–Ocean Dynamics.* Academic Press, 662 pp.

Hasselmann, K., 1962: On the non-linear energy transfer in a gravity-wave spectrum. 1. General theory. *J. Fluid Mech.,* **12,** 481–500.

——, 1963a: On the non-linear energy transfer in a gravity wave spectrum. 2. Conservation theorems–wave-particle analogy–irreversibility. *J. Fluid Mech.,* **15,** 273–281.

——, 1963b: On the non-linear energy transfer in a gravity-wave spectrum. 3. Evaluation of the energy flux and swell-sea interaction for a Neumann spectrum. *J. Fluid Mech.,* **15,** 385–398.

——, 1966: Feynman diagrams and interaction rules of wave-wave scattering processes. *Rev. Geophys.,* **4,** 1–32.

Hibiya, T., Y. Niwa, and K. Fujiwara, 1998: Numerical experiments of nonlinear energy transfer within the oceanic internal wave spectrum. *J. Geophys. Res.,* **103** (C9), 18 715–18 722.

——, M. Nagasawa, and Y. Niwa, 2002: Nonlinear energy transfer within the oceanic internal wave spectrum at mid and high latitudes. *J. Geophys. Res.,* **107,** 3207, doi:10.1029/2001JC001210.

Hinich, M., and C. Clay, 1968: The application of the discrete Fourier transform in the estimation of power spectra, coherence, and

bispectra of geophysical data. *Rev. Geophys. Space Phys.,* **6,** 289–346.

——, and M. Wolinsky, 2005: Normalizing bispectra. *J. Stat. Plann. Inference,* **130** (1–2), 405–411.

Kim, Y., and E. Powers, 1979: Digital bispectral analysis and its applications to non-linear wave interactions. *IEEE Trans. Plasma Sci.,* **7,** 120–131.

Klymak, J., and Coauthors, 2006: An estimate of tidal energy lost to turbulence at the Hawaiian Ridge. *J. Phys. Oceanogr.,* **36,** 1148–1164.

——, R. Pinkel, and L. Rainville, 2008: Direct breaking of the internal tide near topography: Kaena Ridge, Hawaii. *J. Phys. Oceanogr.,* **38,** 380–399.

MacKinnon, J. A., and K. B. Winters, 2005: Subtropical catastrophe: Significant loss of low-mode tidal energy at 28.9°. *Geophys. Res. Lett.,* **32,** L15605, doi:10.1029/2005GL023376.

——, M. Alford, O. M. Sun, R. Pinkel, Z. Zhao, and J. M. Klymak, 2012: Parametric subharmonic instability of the internal tide at 29°N. *J. Phys. Oceanogr,* **43,** 17–28.

McComas, C. H., and F. Bretherton, 1977: Resonant interaction of oceanic internal waves. *J. Geophys. Res.,* **82,** 1367–1412.

——, and P. Müller, 1981a: The dynamic balance of internal waves. *J. Phys. Oceanogr.,* **11,** 970–986.

——, and ——, 1981b: Time scales of resonant interactions among oceanic internal waves. *J. Phys. Oceanogr.,* **11,** 139–147.

Müller, P., and D. Olbers, 1975: On the dynamics of internal waves in the deep ocean. *J. Geophys. Res.,* **80,** 3848–3860.

——, G. Holloway, and F. Henyey, 1986: Nonlinear interactions among internal gravity waves. *Rev. Geophys.,* **24,** 493–536.

Munk, W., 1981: Internal waves and small-scale processes. *Evolution of Physical Oceanography,* B. A. Warren and C. Wunsch, Eds., The MIT Press, 264–290.

——, and C. Wunsch, 1998: Abyssal recipes II: Energetics of tidal and wind mixing. *Deep-Sea Res. I,* **45,** 1977–2010.

Neshyba, S., and E. J. C. Sobey, 1975: Vertical cross coherence and cross bispectra between internal waves measured in a multiple-layered ocean. *J. Geophys. Res.,* **80,** 1152–1162.

Olbers, D., and N. Pomphrey, 1981: Disqualifying two candidates for the energy balance of the oceanic internal wave field. *J. Phys. Oceanogr.,* **11,** 1423–1425.

Phillips, O. M., 1960: On the dynamics of unsteady gravity waves of finite amplitude. *J. Fluid Mech.,* **9,** 193–217.

——, 1961: On the dynamics of unsteady gravity waves of finite amplitude. Part 2. Local properties of a random wave field. *J. Fluid Mech.,* **11,** 143–155.

Pinkel, R., 2008: Advection, phase distortion, and the frequency spectrum of finescale fields in the sea. *J. Phys. Oceanogr.,* **38,** 291–313.

——, and J. Smith, 1992: Repeat-sequence coding for improved precision of Doppler sonar and sodar. *J. Atmos. Oceanic Technol.,* **9,** 149–163.

Polzin, K., 2004: Idealized solutions for the energy balance of the finescale internal wave field. *J. Phys. Oceanogr.,* **34,** 231–246.

——, and Y. V. Lvov, 2011: Toward regional characterizations of the oceanic internal wavefield. *Rev. Geophys.,* **49,** RG4003, doi:10.1029/2010RG000329.

Rainville, L., and R. Pinkel, 2006a: Baroclinic energy flux at the Hawaiian Ridge: Observations from the R/P *FLIP*. *J. Phys. Oceanogr.,* **36,** 1104–1122.

——, and ——, 2006b: Propagation of low-mode internal waves through the ocean. *J. Phys. Oceanogr.,* **36,** 1220–1236.

——, T. M. S. Johnston, G. S. Carter, M. A. Merrifield, R. Pinkel, P. F. Worcester, and B. D. Dushaw, 2010: Interference pattern and propagation of the M_2 internal tide south of the Hawaiian Ridge. *J. Phys. Oceanogr.,* **40,** 311–325.

Rudnick, D. L., and Coauthors, 2003: From tides to mixing along the Hawaiian Ridge. *Science,* **301,** 355–357.

Simmons, H. L., 2008: Spectral modification and geographic redistribution of the semi-diurnal internal tide. *Ocean Modell.,* **21,** 126–138.

St. Laurent, L., and C. Garrett, 2002: The role of internal tides in mixing the deep ocean. *J. Phys. Oceanogr.,* **32,** 2882–2899.

Sun, O. M., and R. Pinkel, 2012: Energy transfer from high-shear, low-frequency internal waves to high-frequency waves near Kaena Ridge, Hawaii. *J. Phys. Oceanogr.,* **42,** 1524–1547.

Wunsch, C., and R. Ferrari, 2004: Vertical mixing, energy, and the general circulation of the oceans. *Annu. Rev. Fluid Mech.,* **36,** 281–314.

Young, W. R., Y.-K. Tsang, and N. J. Balmforth, 2008: Near-inertial parametric subharmonic instability. *J. Fluid Mech.,* **607,** 1–25.

Zhao, Z., and M. Alford, 2009: New altimetric estimates of mode-1 M_2 internal tides in the central North Pacific Ocean. *J. Phys. Oceanogr.,* **39,** 1669–1684.

——, M. H. Alford, J. A. MacKinnon, and R. Pinkel, 2010: Long-range propagation of the semidiurnal internal tide from the Hawaiian Ridge. *J. Phys. Oceanogr.,* **40,** 713–736.